

Resolved stellar mass maps of galaxies. I: method and implications for global mass estimates

Stefano Zibetti^{1*}, Stéphane Charlot², Hans-Walter Rix¹

¹Max-Planck-Institut für Astronomie, Königstuhl 17, D-69117 Heidelberg, Germany

²Institut d'Astrophysique de Paris, CNRS, Université Pierre & Marie Curie, 98 bis Boulevard Arago, 75014 Paris, France

Accepted 2009 August 10. Received 2009 August 10; in original form 2009 April 1

ABSTRACT

We introduce a novel technique to construct spatially resolved maps of stellar mass surface density in galaxies based on optical and near IR imaging. We use optical/NIR colour(s) to infer effective stellar mass-to-light ratios (M/L) at each pixel, which are then multiplied by the surface brightness to obtain the local stellar surface mass density. We build look-up tables to express M/L as a function of colour(s) by marginalizing over a Monte Carlo library of 50,000 stellar population synthesis (SPS) models by Charlot & Bruzual (2007), which include a revised prescription for the TP-AGB stellar evolutionary phase. Moreover, we incorporate a wide range of possible dust extinction parameters. In order to extract reliable flux and colour information at any position in the galaxy, we perform a median adaptive smoothing of the images that preserves the highest possible spatial resolution.

As the most practical and robust, and hence fiducial method, we express the M/L in the H band as a function of $(g-i)$ and $(i-H)$. Stellar mass maps computed in this way have a typical accuracy of 30 per cent or less at any given pixel, determined from the scatter in the models. We compare maps obtained with our fiducial method with those derived using other combinations of band-passes: *i*) mass maps based on the M/L in NIR bands require one optical and one optical-NIR colour to avoid significant biases as a function of the local physical properties of a galaxy; *ii*) maps based on M/L in i band as a function of $(g-i)$ only are generally in excellent agreement with our best optical-NIR set, except for extremely star forming and dust extinguished regions. We further compute stellar mass maps using a model library identical to the previous one except for being based on older SPS models, which assume shorter-lived TP-AGB stars. The M/L in the NIR inferred using these old models may be up to 2.5 times larger than the new ones, but this varies strongly as a function of colours and is maximal for the bluest colours.

Finally, we compare total stellar mass estimates obtained by integrating resolved mass maps with those obtained with unresolved photometry. In galaxies with evident dust lanes, unresolved estimates may miss up to 40 per cent of the total stellar mass because dusty regions are strongly under-represented in the luminous fluxes.

Key words: galaxies:general, stellar content, fundamental parameters, structure, photometry; techniques:image processing, photometric.

1 INTRODUCTION

Stellar mass may be the most fundamental parameter describing present day galaxies. A decade ago Gavazzi et al. (1996) and Gavazzi & Scodreggio (1996) pointed out that the structure and star formation history of disk galaxies are tightly linked with stellar mass. Scodreggio et al. (2002) ex-

tended this observation to all morphologies. The advent of the Sloan Digital Sky Survey (York et al. 2000) and improved stellar population models to estimate stellar masses, ages and metallicities have allowed to put previous claims on a more secure and detailed ground, establishing the dependence of structure, star formation and chemical enrichment histories on stellar mass (e.g. Kauffmann et al. 2003b; Tremonti et al. 2004; Gallazzi et al. 2005). More recently, van den Bosch et al. (2008) have shown that stellar mass

* E-mail: zibetti@mpia.de

also is the main parameter determining the properties of “satellite” galaxies, almost irrespective of their parent dark matter halo mass or of the halo-centric distance: in other words, stellar mass is by far more crucial for predicting, or setting, galaxy properties than environment.

Bell & de Jong (2000) pointed out that the mean stellar mass density of a galaxy may be an even more basic parameter than the total stellar mass in determining the stellar populations in spiral galaxies. This conclusion has been confirmed by Kauffmann et al. (2003b) and extended to all morphological types using more than 100,000 galaxies from the SDSS. Stellar masses for most of these results were derived from spectra or colours that were averaged across much of the stellar bodies of the galaxies, arriving at a global mass-to-light (M/L) ratio estimate.

In the light of these results, it is manifestly important to *i*) test the accuracy of total stellar mass estimates and *ii*) develop methods that actually map the stellar mass surface density distribution in galaxies, rather than just inferring it from single pass-band images rescaled by a uniform mass-to-light ratio. Accurate maps of stellar mass distribution of galaxies are also of fundamental importance for dynamical studies aiming at disentangling the role of secular vs. environmental induced evolution (e.g. Kendall et al. 2008, Foyle et al. 2009 in preparation).

Nowadays a wealth of multi-wavelength imaging is available for large regions of the sky, covering from the UV to the optical, near and mid IR. While most of the multi-wavelength work on galaxies has focused on modeling the total or area-averaged spectral energy distribution, we propose here to combine the photometric information on a pixel-by-pixel level in order to retain the maximum spatial resolution¹. With this method we primarily aim at studying the stellar mass distribution within galaxies but we also aim to study the dependence of the spectral energy distribution on stellar mass density.

Past work has often attempted to map stellar mass distributions within galaxies, resorting to NIR images as a proxy (e.g. Elmegreen & Elmegreen 1984; Rix & Zaritsky 1995; Seigar & James 1998; Grosbøl et al. 2004). More recently, Kendall et al. (2008) have studied the spiral density waves in M81 using three different methods to estimate stellar mass surface density from K_s -band images alone, from 0.8 μm (I band) images with a pixel-by-pixel M/L correction based on $B - V$ colours (Bell & de Jong 2001), and based on Spitzer 3.6+4.5 μm imaging.

In this work we develop a rigorous method to derive spatially resolved stellar mass density maps, based on sets of optical/NIR images of galaxies. The basic idea is that at each position in a galaxy the surface density of stellar mass is given by

$$\Sigma_{M_*}(\alpha, \delta) = \Sigma_\lambda(\alpha, \delta) \Upsilon_\lambda(\alpha, \delta) \quad (1)$$

where $\Sigma_\lambda(\alpha, \delta)$ and $\Upsilon_\lambda(\alpha, \delta)$ are the surface brightness and the *effective* stellar mass-to-light (M/L) ratio in a pass-band of effective wavelength λ . In turn, Υ_λ can be expressed as a function of one or more colours, as measured at the given location in the galaxy. By “effective” M/L ratio we mean

the ratio between stellar mass and the light that reaches the observer, as opposed to the light that is emitted and can possibly be absorbed by the dust inside the galaxy.² In Section 2 we derive the recipes that allow us to express M/L as a function of colours, based on a Monte Carlo library of last generation stellar population synthesis models (i.e. the 2007 version of the models by Bruzual & Charlot 2003), which also include physically motivated prescriptions that account for dust absorption. As we will show, in order to derive M/L that are accurate within ≈ 30 per cent, colour(s) must be accurate at 0.1 magnitude or better. This requires for each resolution element (pixel) a signal-to-noise ratio (S/N hereafter) of $\gtrsim 20$. While typical imaging surveys, like the SDSS and medium-depth observation in the NIR, can easily warrant such S/N for the central and brightest pixels of a galaxy, for lower surface brightnesses ($\mu_r \gtrsim 23\text{mag arcsec}^{-2}$, typically for $R \gtrsim R_e$) this condition cannot be met for individual pixels. Image smoothing allows to enhance the S/N , but at expenses of the effective image resolution. For this reason, we have developed an adaptive median smoothing code (ADAPTSMOOTH, Zibetti 2009 in preparation) that preserves the maximum spatial information compatible with minimum S/N requirements. The image processing required to compute stellar mass maps is detailed in Section 4.

The goal of this paper is mainly to introduce this new method of stellar mass density mapping based on optical and near-IR imaging. Therefore, we limit our sample to only nine galaxies, which span, however, a large range in morphologies. Our selection criteria and the sources of imaging data are presented in Section 3. Despite the small sample size, we find the very interesting result that total stellar masses estimated from resolved and from unresolved photometry differ quite significantly, as we discuss in Section 5.3. A summary with concluding remarks and an outlook of future work is given in Section 6.

2 METHODOLOGY (I): STELLAR POPULATION SYNTHESIS MODELS

2.1 Stellar M/L from optical-NIR colours

In this Section we combine stellar population synthesis (SPS) models with simple prescriptions for dust attenuation to devise a set of look-up tables that allow us to estimate the effective stellar mass-to-light ratio given either one or two optical/NIR colours. As mentioned above, by “effective” M/L we mean the ratio between stellar mass and the light that reaches the observer, after being possibly absorbed by the dust within the galaxy. To generate our fiducial SPS models we adopt the 2007 version of Gissel (Bruzual & Charlot 2003, CB07 hereafter), which includes revised prescriptions for the TP-AGB evolutionary phase, following Marigo & Girardi (2007) and Marigo et al. (2008)³.

² Emission lines from the gaseous interstellar medium can affect the “effective” M/L as well. We will not take their contamination into account explicitly, but only implicitly by not using passbands that include the $\text{H}\alpha$ emission.

³ Using simple stellar populations of different metallicities we have compared the M/L ratios in red and NIR bands as a function of colours predicted by CB07 and Maraston (2005) models.

¹ Pioneering work in the pixel-by-pixel approach was already conducted by Abraham et al. (1999) and Conti et al. (2003).

An accurate modeling of this phase is of particular relevance to correctly predict fluxes (hence colours and M/L) that involve the wavelength range between 1 and 2.5 μm for stellar populations of ages between 0.3 and 2 Gyr (e.g. Maraston 2005; Bruzual 2007). The emerging optical/NIR colour(s) of the stellar population at a given position in a galaxy are determined by a variety of factors, namely the star formation history, the metallicity, the amount, spatial distribution and optical properties of dust and the initial mass function (IMF) of stars. In the following we will work under the assumption that the IMF is universal and well described by Chabrier (2003). The systematic effects on mass estimates induced by different choices of IMF (e.g. Bell & de Jong 2001) are not of primary relevance here, as long as the IMF can be considered uniform within a galaxy. This assumption is suggested by Occam’s razor, as we lack any way of linking possible variation of IMF to local observables within a galaxy.

All other relevant parameters, star formation history, metallicity, dust, are expected to vary significantly from place to place in a galaxy. To explore the effect of such differences on colours and M/L , we build a Monte Carlo library of SPS models with the following properties, as in Kong et al. (2004) and da Cunha et al. (2008). Each stellar population has a fixed metallicity, randomly chosen between 0.02 and 2 times solar, and a two-component star formation history (SFH), consisting of a continuous, exponentially declining mode with random bursts superimposed. We follow Kauffmann et al. (2003a) to parameterize each SFH by a set of variables with a given prior probability distribution. The effect of dust is modeled according to the formalism introduced by Charlot & Fall (2000) to treat the differential absorption by dust in the short-lived birth clouds and in the interstellar medium (ISM). As in da Cunha et al. (2008), the two parameters that govern dust absorption, the total effective V -band optical depth $\hat{\tau}_V$ and the fraction contributed by dust in the ambient ISM μ , have $1 - \tanh$ prior probability distributions, such that $\hat{\tau}_V$ is approximately uniform over the interval from 0 to 4 and drops exponentially to zero around $\hat{\tau}_V = 6$, while μ is approximately uniform over the interval from 0 to 0.6 and drops exponentially to zero around 1. For each model emerging fluxes and stellar masses are combined to compute colours and effective M/L ratios.

To study how M/L in a given band depends on colours we adopt a marginalization approach. We bin models in the 1- or 2-dimensional colour space we aim at studying, with a bin width $\lesssim \sigma_{\text{colour}}$, the typical observational error. Specifically, we adopt a bin width of 0.05 mag in each colour dimension. Within each bin we compute the median M/L and the logarithmic *r.m.s.* from all parameter combinations that lead to those colours. This approach incorporates uncertainties from parameter degeneracies or model simplifications. E.g. the assumption of a single metallicity in a given SPS model may be unrealistic even on local scales, but by marginalizing over a large number of random models with

different metallicities we indirectly take varying metallicity into account.

In principle, more colours should provide better constrained stellar populations and hence M/L ; in practice, there are limitations: most of the colour information is nearly degenerate, especially that from adjacent bands like $r - i$ and $i - z$. We have found that using one more colour just complicates the analysis by increasing its dimensionality without reducing the M/L uncertainty. More colours would only provide improvements if the systematic flux uncertainties in the models were smaller than 10 per cent, which current models do not reach yet. For these reasons we limit our study to two colour indexes at most.

For practical reasons, we only consider broad passbands with extensive existing data sets: the SDSS (u , g , r , i and z) and the J , H , K filters in the NIR. Among them, we discard the u band because of the typically low S/N in SDSS and the very high dust attenuation that can lead to almost complete obscuration over a significant area of a galaxy. We further discard the r band because of the strong local contamination by $H\alpha$ emission in HII regions: typical equivalent widths of a few hundreds Ångströms in those regions would lead to overestimate the stellar emission by up to 0.5 mag in r . Among the three NIR bands we focus on the H as our reference band, but we note that any conclusion we present regarding this band applies almost identically to J and K as well.

It is well known from previous studies (e.g. Rix & Zaritsky 1995 appendix B, or Bell & de Jong 2001) that in NIR bands M/L variations as a function of stellar population parameters are smaller than at shorter wavelengths, because the bulk of long-lived low-mass stars dominate the emission in the NIR. Moreover, dust extinction is lower at longer wavelengths. Thus, for our fiducial mass reconstruction method it is natural to choose a NIR band (namely the H band) as the “luminance” band, whose surface brightness we want to convert to stellar mass surface density. As for the colour space where we map M/L we choose $(g - i)$ - $(i - H)$, because these colours provide the largest wavelength leverage and thus the highest sensitivity to stellar population and dust properties. This large leverage also minimizes the effect of any systematic uncertainties in the photometric calibration of SPS models or of the imaging data: 10 per cent flux uncertainties are negligible for a colour range of 2 mag, but not for a range of a few 0.1 mag. From now on, magnitudes in the SDSS bands are meant to be in the AB system, while for Johnson-Cousins filters they are expressed in Vega units. Colours that involve SDSS and Johnson-Cousins pass-bands, are computed by subtracting the magnitudes in the two respective systems such that, e.g., $i - H$ means $i_{\text{AB}} - H_{\text{Vega}}$.

The top right panel of Figure 1 shows Υ_H , the M/L ratio in H -band in solar units, as a function of $(g - i)$, $(i - H)$ colours, based on the Monte Carlo library of SPS models. Our models cover a broad sequence from blue (lower left corner) to red (upper right corner) across the colour-colour diagram, with Υ_H increasing from $10^{-1.5}$ to $10^{0.8}$, i.e. by a factor 200. It is apparent that the $g - i$ colour is the main predictor of the trend in Υ_H , which increases by 0.08 dex per 0.1 mag in $g - i$. However, for a given $g - i$ a range of Υ_H is allowed. This is quantified in the top left panel of Figure 1, where we plot (solid line) the median Υ_H as a function of $g - i$ (binned in 0.05 mag). Dash-dotted lines show the maximum

Although significant discrepancies up to a few tenths of a dex are seen, especially at the youngest ages, in the most relevant range of colours ($g - i > 0.2$ mag, see Sect. 4.2) no systematic offset is observed.

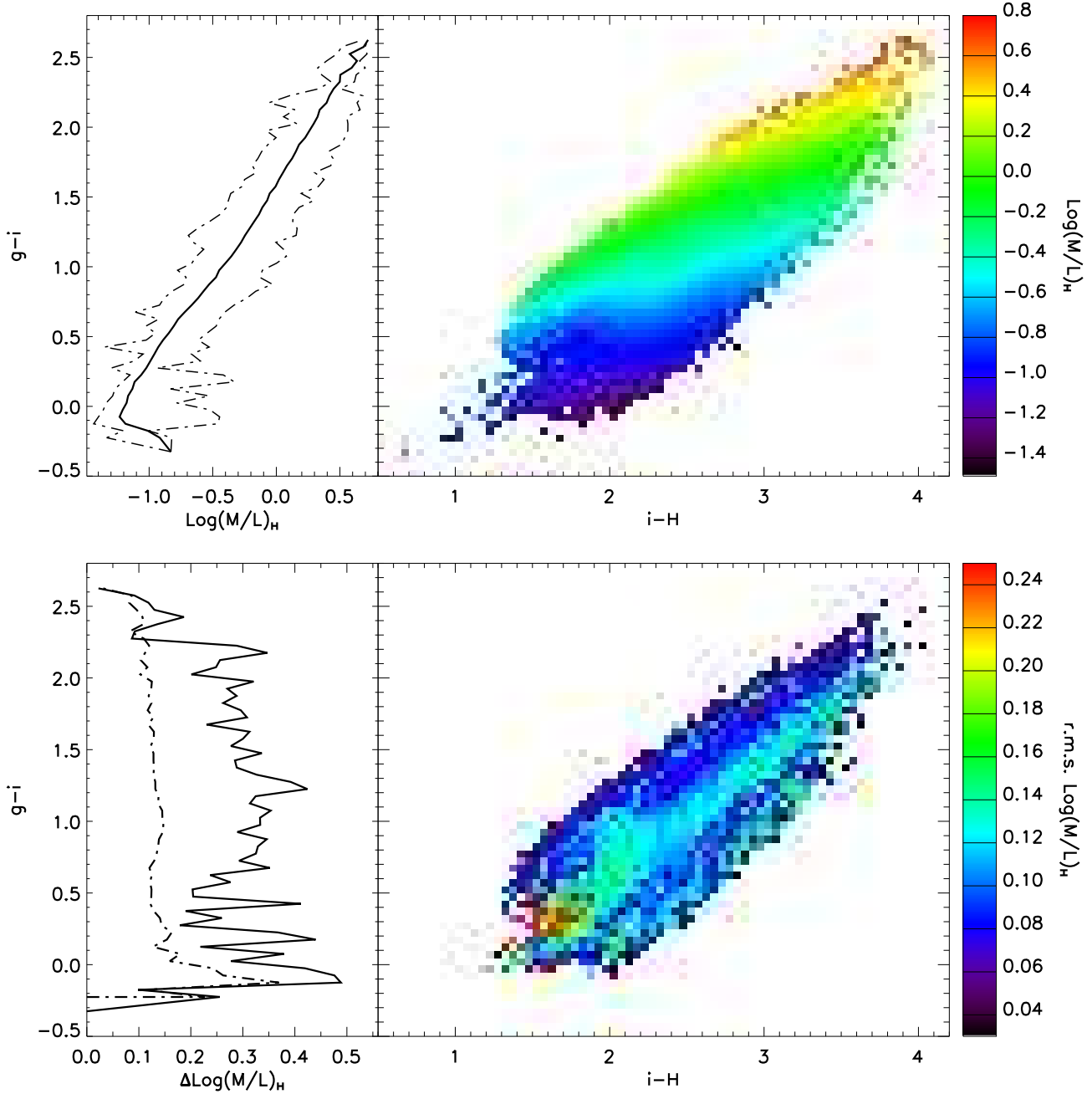


Figure 1. Effective mass-to-light ratio in H band as a function of colours in the Monte Carlo library based on CB07 SPS models. *Top panels:* right the median $\log \Upsilon_H$ for models binned $0.05 \times 0.05 \text{ mag}^2$ in the $(i-H) - (g-i)$ colour-colour space. Left: the median $\log \Upsilon_H$ for the same models binned 0.05 mag in $(g-i)$ only (solid line), and the minimum and maximum value of $\log \Upsilon_H(i-H, g-i)$ along each row of the right panel (dash-dotted lines). *Bottom panels:* right, the *r.m.s.* of $\log \Upsilon_H$ for models binned $0.05 \times 0.05 \text{ mag}^2$ in the $(i-H) - (g-i)$ colour-colour space. Left: the solid line shows the half-range of values of $\log \Upsilon_H$ as a function of $g-i$ from the top right panel, compared to the mean *r.m.s.* of $\log \Upsilon_H$ in individual colour-colour cells (dash-dotted line).

and minimum Υ_H taken from the right-hand panel, for a given $g-i$: the spread in Υ_H is between 0.5 and 1 dex for most of $g-i$ values, showing that the additional information from the second colour, $i-H$, is crucial to minimize the uncertainty in Υ_H .

Even in the 2-dimensional colour space the remaining scatter of the predicted Υ_H at a given $(i-H)$, $(g-i)$ is significant. The *r.m.s.* of $\log \Upsilon_H$ is represented in the colour-colour space in the bottom right panel of Figure 1. The typical *r.m.s.* ranges between 0.05 and 0.15 dex (i.e., between 10 and 40 per cent approximately) and is thus comparable to the effect of errors on colours of ≈ 0.1 mag, except for the region occupied by “blue” models ($g-i < 0.7 \wedge i-H < 2.2$). Models in this region are characterized by relatively young stellar populations with a strongly varying NIR emission (in particular by TP-AGB stars, see also Section 2.2), which produce *r.m.s.* scatter up to 0.25 dex (approximately a factor 1.8). It is interesting to see how this scatter in $\log \Upsilon_H(g-i, i-H)$ compares with the half-range of $\log \Upsilon_H(g-i)$ that we derived from the top right panel of Fig. 1. The latter can be considered an estimate of the typical error that one makes by replacing $\log \Upsilon_H(g-i, i-H)$ by the median $\log \Upsilon_H(g-i)$. The bottom left panel of Fig. 1 shows that for most $g-i$ the mean *r.m.s.* scatter in $\log \Upsilon_H(g-i, i-H)$ at any given $g-i$ (dash-dotted line) is ≈ 0.1 dex, while it is ≈ 0.3 dex for $\log \Upsilon_H(g-i)$ (solid line). Through the use of two colours to determine the M/L ratio one can reduce the uncertainties from a factor 2 to a factor 1.25.

It is worth noting that the choice of prior parameter distributions in the model library can affect the estimated median M/L for a given colour (pair). The time elapsed since the beginning of star formation, t_{form} , and the time and intensity of bursts are the parameters whose distributions affect most the median M/L because the fraction of mass hidden in old, low-luminosity stars critically depend on these parameters. As an extreme case, we test the effect of removing from our library all models with $t_{\text{form}} < 10$ Gyr. As expected, the models with larger t_{form} predict larger M/L . The largest differences (from 0.1 up to 0.4 dex) with respect to our default library are found for $g-i < 0.6$ and for the very reddest models in $i-H$ at given $g-i$. As it is shown in Section 4.2 and Fig. 6, these regions of the colour-colour space are only sparsely populated in the observations. The rest of the space is only marginally affected (typically 0.02 dex difference, increasing toward the extreme regions mentioned before). We conclude that our choice of prior is not critical when we use two colours. However, it can gain greater relevance if only one colour is used, as we show in section 2.4. In Appendix A we show and discuss the detailed distributions of the physical parameters that characterize the models as a function of colours. In particular, we note that extremely red colours ($g-i > 1.5$) and correspondingly very high Υ_H (up to 5-6) can be produced only by models with total dust optical depth $\hat{\tau}_V \gtrsim 3$.

2.2 Comparison with models using an older TP-AGB star prescription (BC03)

Most recent works in stellar population synthesis models agree on the relevance of the TP-AGB phase for a correct estimate of the NIR flux of stellar populations at ages between 0.3 and 2 Gyr (e.g. Maraston 2005; Bruzual 2007). Yet, a

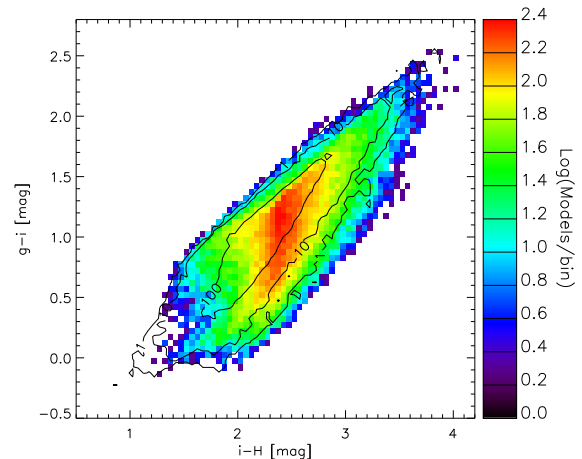


Figure 2. Prior distribution of models in $(i-H) - (g-i)$ colour-colour space: the colour map shows the distribution for the CB07 library, solid contours are for BC03 (1, 10 and 100 models per colour-colour bin). The effect of the revised prescription for TP-AGB stars is evident in the shift of the CB07 models to redder $i-H$ values with respect to BC03.

fully reliable quantification of this effect is still under debate. In order to illustrate the impact of different prescriptions for the TP-AGB phase (in particular, those concerning its duration) we compare M/L determinations from our standard CB07 models with those derived from the BC03 models (Bruzual & Charlot 2003), which assume much shorter-lived TP-AGB stars. We have produced a library of SPS models with identical star formation history, metallicity, IMF and dust properties as described before, but using the stellar evolutionary tracks and libraries of BC03.

In Figure 2 we compare the distribution of the two model libraries in the $(i-H) - (g-i)$ colour-colour space. The intensity scale in colour shows the distribution of our default library CB07, while the distribution of BC03 models is shown by the overlaid contours. The effect of the revised TP-AGB star prescriptions in CB07 is mainly to move blue models ($i-H < 2$, $g-i < 1$) to redder $i-H$. Other regions of the colour-colour space are only slightly affected by TP-AGB stars, the only significant difference being a ~ 0.2 mag more extended tail at higher $i-H$ for a given $g-i$.

What is most interesting for M/L estimates is the systematic difference between the two libraries as a function of the observables, i.e. the colours, which is illustrated in Figure 3. In the right panel different colour shadings shows the logarithmic difference of the median $\log \Upsilon_H$ between CB07 and BC03. The original colour space coverage of the two libraries is displayed by the solid (CB07) and dashed (BC03) contours. Outside the original coverage (regions where only one of the two libraries has models) the M/L is extrapolated using a minimum curvature fitting algorithm. As expected, the largest differences are found for the bluest colours ($g-i < 0.7 \wedge i-H < 2.2$), that correspond to young ($t < 2$ Gyr) stellar populations, where the NIR emission is strongly influenced by TP-AGB stars. At those colours typical systematic differences between CB07 and BC03 models are between -0.25 and -0.4 dex, i.e. the old SPS models that assume short-lived TP-AGB stars imply higher masses, by a factor ≈ 2 . The rest of the colour space is only slightly

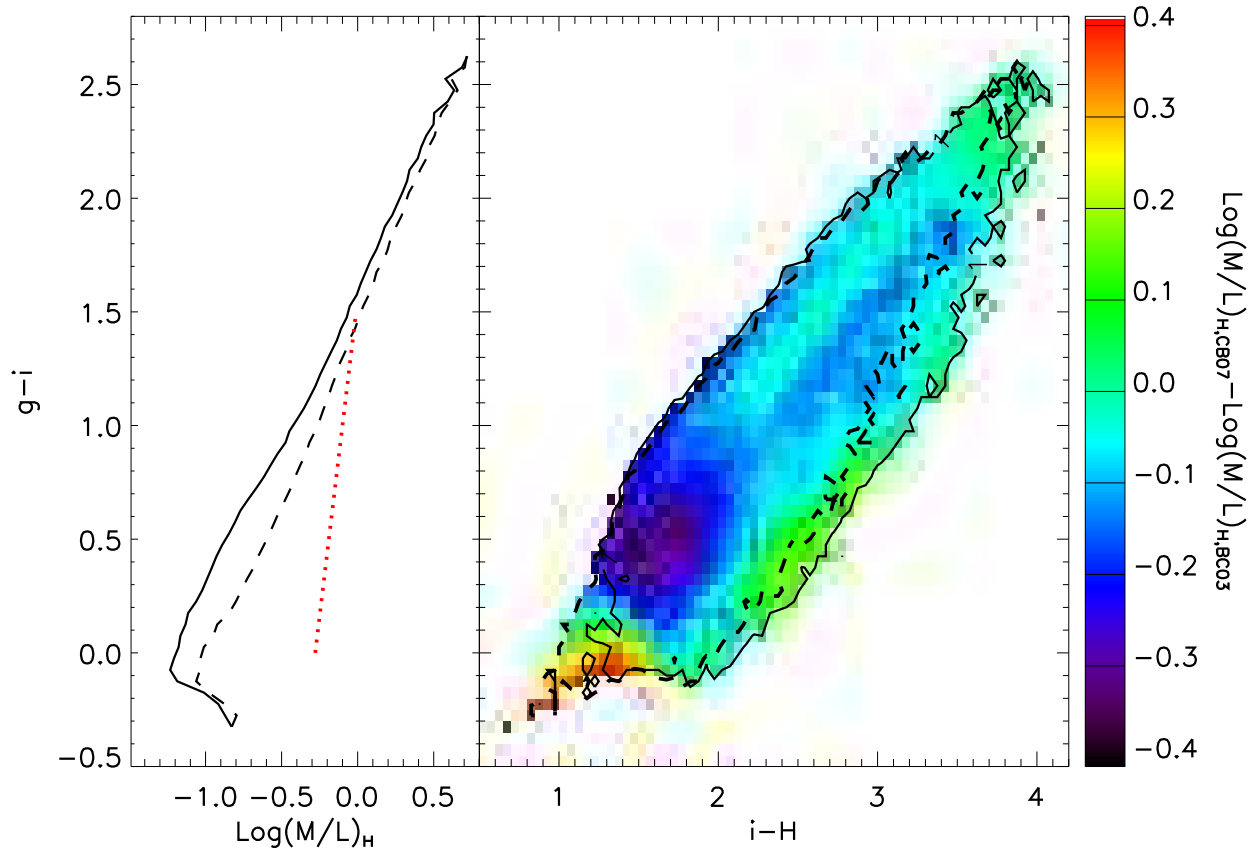


Figure 3. Comparison between CB07- and BC03-based libraries. *Right panel:* difference of median $\log \Upsilon_H$ derived using CB07 and BC03 models, binned $0.05 \times 0.05 \text{ mag}^2$ in $(i-H) - (g-i)$. Black contours show the distribution of models in colour-colour space for CB07 (solid contours) and BC03 (dashed). CB07 models, which include longer-lived TP-AGB stars, appear to extend more to red $i-H$ than BC03, with an overall shift towards redder $i-H$ at low $g-i$, due to young stellar populations which include a significant fraction of TP-AGB. *Left panel:* median $\log \Upsilon_H$ as a function of $g-i$ for CB07- and BC03-based models, shown as solid and dashed lines, respectively. The old BC03 models with shorter-lived TP-AGB stars overestimate Υ_H by several tenths of dex in blue/young stellar populations, with respect to the new CB07. The red dotted line represents the power-law fitting formula from Bell et al. (2003).

affected, with typical differences between 0 and -0.1 dex (20 per cent). It is worth noting that over all the colour space (with the only exception of a few marginal regions) CB07 models predict lower M/L in the NIR than BC03. This systematic offset is also illustrated in the left panel of Fig. 3, where the median $\log \Upsilon_H(g-i)$ is shown for CB07 and BC03 as solid and dashed lines, respectively.

2.3 M/L from optical bands only

The modeling uncertainties inherent to NIR pass-bands motivated us to test the accuracy of M/L determination using optical pass-bands and colours only. For this test we adopt the SDSS i band for luminance and study the dependence of Υ_i on $(g-i, i-H)$ (as in the previous section) and then as a function of $g-i$ only⁴.

In the right panel of Figure 4 we show the effective M/L in i band as a function of the two optical/NIR colours $g-i$,

$i-H$. The comparison with the analogous plot of Fig. 1 shows two main differences: the range of M/L in i is almost ten times larger than in H band, but the dependence of Υ_i on $(i-H)$ is extremely weak. In the left panel we compare the median $\log \Upsilon_i(g-i)$ (solid black line) to the full range of Υ_i (black dot-dashed lines) at a given $(g-i)$. The min-max half range is typically 0.15 dex, comparable to the *r.m.s.* in individual cells in the $(g-i, i-H)$ colour-space that one can derive from the bottom right panel of Fig. 1.⁵ In the left panel of Fig. 4 we also plot with grey lines median, minimum and maximum $\log M/L$ as obtained from BC03 models. The systematic difference to CB07 models in this case is 0.1 dex at most, to be compared with differences of up to 0.4 dex in H -band (see paragraph 2.2).

In the light of these results, the use of i -band images for luminance and $g-i$ maps to extract Υ_i appears as an attractive alternative to our fiducial method, the use of H -band with $(g-i, i-H)$ colours. While H -band with $(g-i, i-H)$

⁴ We have conducted the same test using the SDSS z band instead of i and obtained qualitatively identical results.

⁵ The *r.m.s.* of $\log \Upsilon_i(g-i, i-H)$ is the same as for $\log \Upsilon_H(g-i, i-H)$ because in each cell the luminosity ratio in i and H band is fixed by the $i-H$ colour.

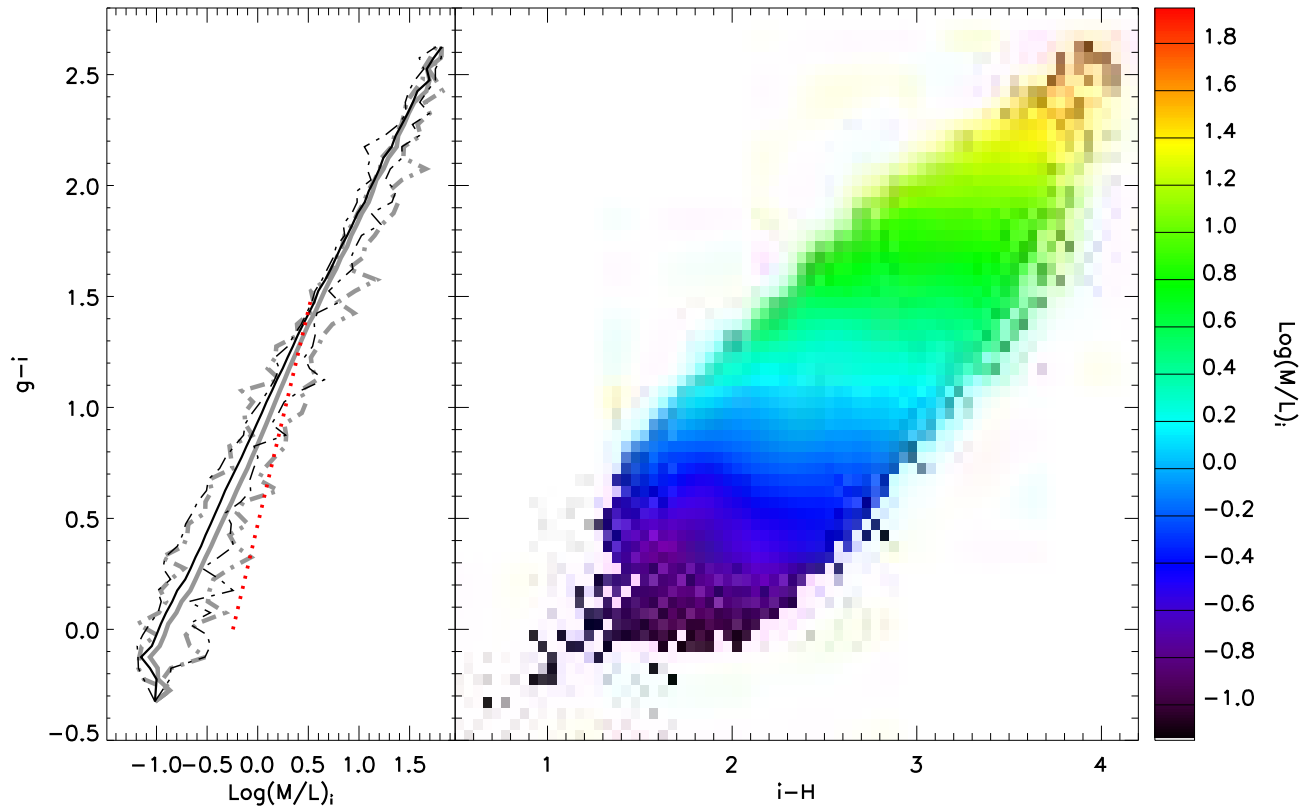


Figure 4. Effective mass-to-light ratio in i band as a function of colours in the Monte Carlo library based on CB07 SPS models. *Right panel:* the median $\log \Upsilon_i$ for models binned $0.05 \times 0.05 \text{ mag}^2$ in the $(i-H) - (g-i)$ colour-colour space. *Left:* the median $\log \Upsilon_i$ for the same models binned 0.05 mag in $(g-i)$ (solid line), and the minimum and maximum value on $\log \Upsilon_i$ along each row of the right panel (dash-dotted lines). Black lines represent CB07 models, while grey lines display BC03. The red dotted line is the Bell et al.’s (2003) power-law fit.

is more accurate and stable against photometric errors because of the smaller range in Υ_H , the use of i and g band is certainly cheaper in terms of observational resources and less sensitive to the still controversial modeling of TP-AGB stars. However, in Section 5 we show that the use of NIR is the only sensible way to go in two regimes: *i*) in presence of heavy dust obscuration, where radiation at shorter wavelengths will not emerge, and *ii*) in the case of very young stellar populations that completely dominate the optical light.

2.4 Comparison with Bell et al. (2003)

A one-colour method similar to the one we adopt to derive $\Upsilon_i(g-i)$ and $\Upsilon_H(g-i)$ was formerly developed by Bell & de Jong (2001) and subsequently revised by Bell et al. (2003). In Appendix A2 of their paper they give power-law fits for M/L in different optical and NIR bands as a function of one optical colour. In Fig. 3 and 4 we plot the Bell et al.’s relations for $\Upsilon_H(g-i)$ and $\Upsilon_i(g-i)$, respectively, as red dotted lines, limited to the colour range actually covered in their work. We have scaled down their M/L by -0.093 dex to take the difference between our Chabrier IMF and their scaled Salpeter IMF (Gallazzi et al. 2008). Their M/L agree with ours only for the reddest $(g-i)$ corresponding

to old unextincted stellar population. Yet, the dependence on $(g-i)$ is much weaker according to Bell et al.’s fits and results in large discrepancies at the blue end of the distribution, where they predict M/L approximately ten times larger than ours. The same systematic variations occur in all bands and colours analyzed in Bell et al. (2003), as can be verified using the power-law fits derived from our fiducial models which are given in Table B1 in Appendix B.

There are in fact a number of differences between our methodology and Bell et al.’s. First of all, their models are based on BC03 SPS models. However, Figures 3 and 4 show that large discrepancies are present also in comparison to our BC03-based estimates. Bell et al. (2003) do not explicitly take dust into account and, more importantly, only consider relatively smooth star formation histories, starting 12 Gyr in the past and with a maximum stellar mass contribution from burst in the last 2 Gyr smaller than 10 per cent. As opposed, we do model the effect of dust up to optical depth of $\hat{\tau}_V \approx 6$ and, more importantly, in our library we allow young ages (of a few Gyr) and have a large fraction of star formation bursts, which are the main cause of our lower M/L for young stellar populations (see e.g. Fig. 5 of Bell & de Jong 2001, and Sec. 2 above), especially when one colour only is used. On the local scales that we want to study, both

dust and bursty star formation histories cannot be neglected. This is easy to realize just looking at the true colour images of common spiral galaxies, where dust reddened regions are seen and young OB associations dominate in spiral arms. Therefore we argue that our models are better suited to describe SEDs on local scales than Bell et al.’s. This may not be the case if galaxies are considered globally: in fact for “normal” galaxies, global star formation histories are likely to be much smoother and dust is not expected to play a major role (except for edge-on disks). We explore this issue further in Section 5.3.

3 SAMPLE AND IMAGING DATA

To test our mass map reconstruction we select a small sample of nearby galaxies that span a broad range of morphologies and physical properties and for which a wealth of high-quality multi-wavelength imaging is available. We draw our sample from the Spitzer Infrared Nearby Galaxies Survey (SINGS Kennicutt et al. 2003), a comprehensive imaging and spectroscopic study of 75 nearby galaxies ($D < 30$ Mpc) conducted in the IR with the Spitzer Space Telescope, for which coordinated observations at visible, near-IR, ultraviolet, and radio wavelengths are either already in place or planned. Complementing this unique dataset with high-quality stellar mass maps will provide key insights into the physics of galaxies and, at the same time, will allow us to test our method in the best characterized physical conditions. Among the 75 SINGS galaxies we select 9 for which SDSS and medium/deep near-IR (1-2.5 μm) imaging is available. The latter is taken either from GOLD Mine (Gavazzi et al. 2003), a large database that provides NIR images of 1568 galaxies (mainly in the Virgo cluster and the Coma supercluster), or from the 3rd data release of UKIDSS (Lawrence et al. 2007, Warren et al., in preparation), that uses the UKIRT Wide Field Camera (WFCAM Casali et al. 2007).

The 9 galaxies are listed in Table 1 with their NGC name (column 1), coordinates (col. 2 and 3) and morphological type (col. 4) according to the RC3 catalog (de Vaucouleurs et al. 1991). Distances are reported in column 5. Seven out of the nine galaxies belong to the Virgo cluster and, following Gavazzi et al. (1999), we assign them a distance of 17.1 Mpc. For the other two galaxies we use distances as given by NED based on their measured redshift, assuming $H_0 = 73 \text{ km sec}^{-1} \text{ Mpc}^{-1}$. Based on the computed distance and the pixel scale of the different detectors we compute also the angular scale (col. 6) and pixel scale (col. 7): for the median seeing of $\approx 1.4''$, we could resolve physical scales of $\approx 120 \text{ pc}$ in all cases, although the pixel scales range from 18 to 132 pc. We use H as NIR band except for NGC 4569, for which only K_s is available. Our sample includes one elliptical galaxy, two early type Sab spirals, one Sb, four Sbc’s (including one peculiar) and one Sc, thus spanning the whole range of morphologies for “normal” (i.e. not irregular) galaxies.

True colour images of the galaxies sorted by morphological type are presented in Figure 5. The NIR band is mapped in the red channel, i band in the green and g in the blue; the three channels are shown in logarithmic intensity scaling and are balanced to show a solar spectral energy distribution as white. The images that we show in Fig. 5 are matched,

calibrated and filtered as explained in Section 4. Each panel reports the physical scale in kpc and a rod whose length corresponds to 50 pixels.

3.1 Image reduction and calibration

Imaging data for this study are taken from three different sources, each requiring slightly different pre-reductions and calibrations, that we describe in this section.

For the optical images (g , i and z bands) we completely rely on the 7th data release of the SDSS (York et al. 2000, Abazajian et al. 2009, in press). SDSS images come in the format of “corrected frames”, that are bias-subtracted, flat-fielded cuts of long imaging scans. Given the relatively large size of our galaxies, in some cases two different scans must be combined. In the general case we reduce each scan separately: first we join the frames, then we compute an accurate astrometric solution using stars from the SDSS catalog. We subtract the sky background by fitting a plane surface to the pixels in a series of boxes that we define around the galaxy, with a typical size of roughly one tenth of the galaxy. The fitted plane is allowed to be tilted in the scan direction only, in order to take temporal background variations into account. The *r.m.s.* of the median background levels among the boxes provide an estimate of the large scale background fluctuations that is used later on to make S/N cuts. If more than one scan is used, we choose a primary scan (where most of the galaxy is contained) and we rescale all secondary scans in intensity according to the difference in photometric zero point (as derived from the SDSS database). Finally, we build a mosaic of the scans based on the previously computed astrometric solutions using SWARP (<http://astromatic.iap.fr/software/swarp>).⁶ We refer the reader to Fukugita et al. (1996); Gunn et al. (1998, 2006); Smith & et al. (2002) for a summary of the properties of the SDSS imaging.

The NIR images from GOLD Mine come as reduced and calibrated coadded images. We compute accurate astrometric solutions for each image by matching i -band selected stars from the SDSS catalogs. Sky subtraction is performed similarly as for SDSS images, but using a constant plane (order 0 surface in both coordinates). Finally we check (and refine where needed) the photometric calibration using stars from 2MASS (Jarrett et al. 2000): the final photometric accuracy (zero point) is typically $\lesssim 0.1 \text{ mag}$. We note that all of the GOLD Mine images used in this work have pixel scales between 1.5 and 1.6 arcsec per pixel, that severely under-sample the PSF. This does not represent a problem for the following analysis though, as a sufficient physical resolution is provided anyway (Table 1).

For UKIDSS images we have used stacks from the 3rd data release, which is described in detail in Warren et al. (in preparation). The pipeline processing and science archive are described in Irwin et al. (2009, in preparation) and Hambly et al. (2008). Sky subtraction and astrometric calibrations are performed exactly as for GOLD Mine images. The UKIDSS photometric system is described in Hewett

⁶ The automated procedure to build SDSS mosaics as described here is available as IRAF package at <http://www.mpa.de/homes/zibetti/software/SDSSmosaic.html>

Table 1. The sample

Denomination	RA	Dec	Morph. type	Distance	Angular scale	Pixel scale	NIR	NIR source
(1)	(J2000.0) (2)	(J2000.0) (3)	(4)	Mpc (5)	pc arcsec ⁻¹ (6)	pc pixel ⁻¹ (7)	(8)	(9)
NGC 3521	11h05m48.6s	-00d02m09s	SABbc	9.2	45	18	H	UKIDSS
NGC 4254	12h18m49.6s	+14d24m59s	SAC	17.1	82	132	H	GOLDMine
NGC 4321	12h22m54.9s	+15d49m21s	SABbc	17.1	82	132	H	GOLDMine
NGC 4450	12h28m29.6s	+17d05m06s	SAab	17.1	82	124	H	GOLDMine
NGC 4536	12h34m27.0s	+02d11m17s	SABbc	17.1	82	132	H	GOLDMine
NGC 4552	12h35m39.8s	+12d33m23s	E	17.1	82	33	H	UKIDSS
NGC 4569	12h36m49.8s	+13d09m46s	SABab	17.1	82	132	K _s	GOLDMine
NGC 4579	12h37m43.5s	+11d49m05s	SABb	17.1	82	132	H	GOLDMine
NGC 5713	14h40m11.5s	-00d17m20s	SABbc p	25.9	126	51	H	UKIDSS

et al. (2006), and the calibration is described in Hodgkin et al. (2008). The absolute photometric accuracy is typically around few 0.01 mag. We note that the pixel scale of 0.4 arcsec per pixel perfectly matches SDSS images.

In both GOLD Mine and UKIDSS datasets the typical depth reached by the NIR images used in this study is $\mu_H \approx 20.5$ mag arcsec⁻² (3σ on a square arcsecond).

All fluxes are corrected for Galactic foreground extinction, as given in NED or the SDSS database, which are based on Schlegel et al. (1998).

4 METHODOLOGY (II): FROM MULTI-BAND IMAGES TO MASS MAPS

4.1 Image processing

Images in different bands must be registered and resampled to a common resolution before pixel-by-pixel colour information can be extracted. To do this we use SWARP and the astrometric solutions computed in the previous section. We choose to degrade all sky-subtracted images to the lowest resolution image for each galaxy. In practice, for all images taken from GOLD Mine this translates into degrading the SDSS images to the NIR pixel scale⁷, while the original pixel scale is kept for the UKIDSS data. In principle, images taken with different instruments, in different bands and seeing conditions must also be convolved to a common point spread function (PSF). However we do not apply such convolution, as the PSFs are already similar and a convolution would corrupt the noise properties.

As shown in Sec. 2, colours must be accurate at better to $\lesssim 0.1$ mag to compute M/L ratios that match theoretical uncertainties. In turn, this requires surface brightness in each band to be accurate within ≈ 0.05 mag, or $S/N \gtrsim 20$ per pixel. The noise budget includes local photon noise, assumed to be Gaussian, and background fluctuations that may become the dominant source of uncertainty at low surface brightness.

Local photon noise can be reduced to the required level with low-pass filters, using a smoothing kernel of sufficiently large size. However, a fixed-width kernel produces a uniform

degradation of the effective spatial resolution of the entire image, including bright regions of the galaxy where no or minimal smoothing is required. For this reason we have implemented a new code to perform image smoothing with a variable kernel, whose size is adapted to the local S/N . This code is called ADAPTSMOOTH and will be presented in detail in a forthcoming paper (Zibetti 2009, in preparation). Briefly, the idea is to replace the intensity in each pixel with the median intensity in a circle of radius R of surrounding pixels, where R is determined as the minimum radius required to attain the minimum S/N of 20. The procedure works by increasing R iteratively. If the minimum S/N of 20 cannot be reached even with the maximum smoothing radius R_{\max} , the pixel is flagged and assigned a value of 0. In this work we adopt $R_{\max} = 13$ pixels for the GOLD Mine images (corresponding to 20 arcsec) and 20 for the UKIDSS (corresponding to 8 arcsec). In this way the full spatial resolution is preserved in the brightest regions of a galaxy, while increasingly strong smoothing is applied to lower and lower surface brightness regions.

ADAPTSMOOTH is run a first time on the individual images in each band. A mask that contains the smoothing radius for each pixel (or an overflow value where the required S/N cannot be reached within R_{\max}) is output for each image. In order to match the spatial resolution between all three bands we combine the masks into a common mask with the maximum of the three smoothing radii at a given position. We then apply an intensity cut to take into account large scale background fluctuations, as computed from the sky box statistics. All pixels with an intensity in the smoothed image less than 10 times the large scale background fluctuation *r.m.s.* in one of the three bands are flagged with the overflow value in the mask. Furthermore we manually edit the mask to flag stars and other interlopers. With this mask we re-run ADAPTSMOOTH in all bands in “input mask” mode, that is using the smoothing radii as given in the input mask. In pixels where the overflow value is set, a default value for undefined is output. The adaptively smoothed images that result from this procedure are shown in the three-colour composite images of Figure 5. We note that *i*) the NIR images put the strictest constraints for smoothing and intensity cuts; *ii*) the intensity cut we adopt here is less strict than required to ensure $S/N > 20$ at all positions and can produce systematic colour offsets. However, the intensity threshold in the NIR in all cases is so high that background fluctuations in the optical are negligible in the

⁷ In order to correctly propagate the noise properties of the images while degrading the resolution it is important to run SWARP with an oversampling factor equal to the ratio between the final and the original pixel scale.

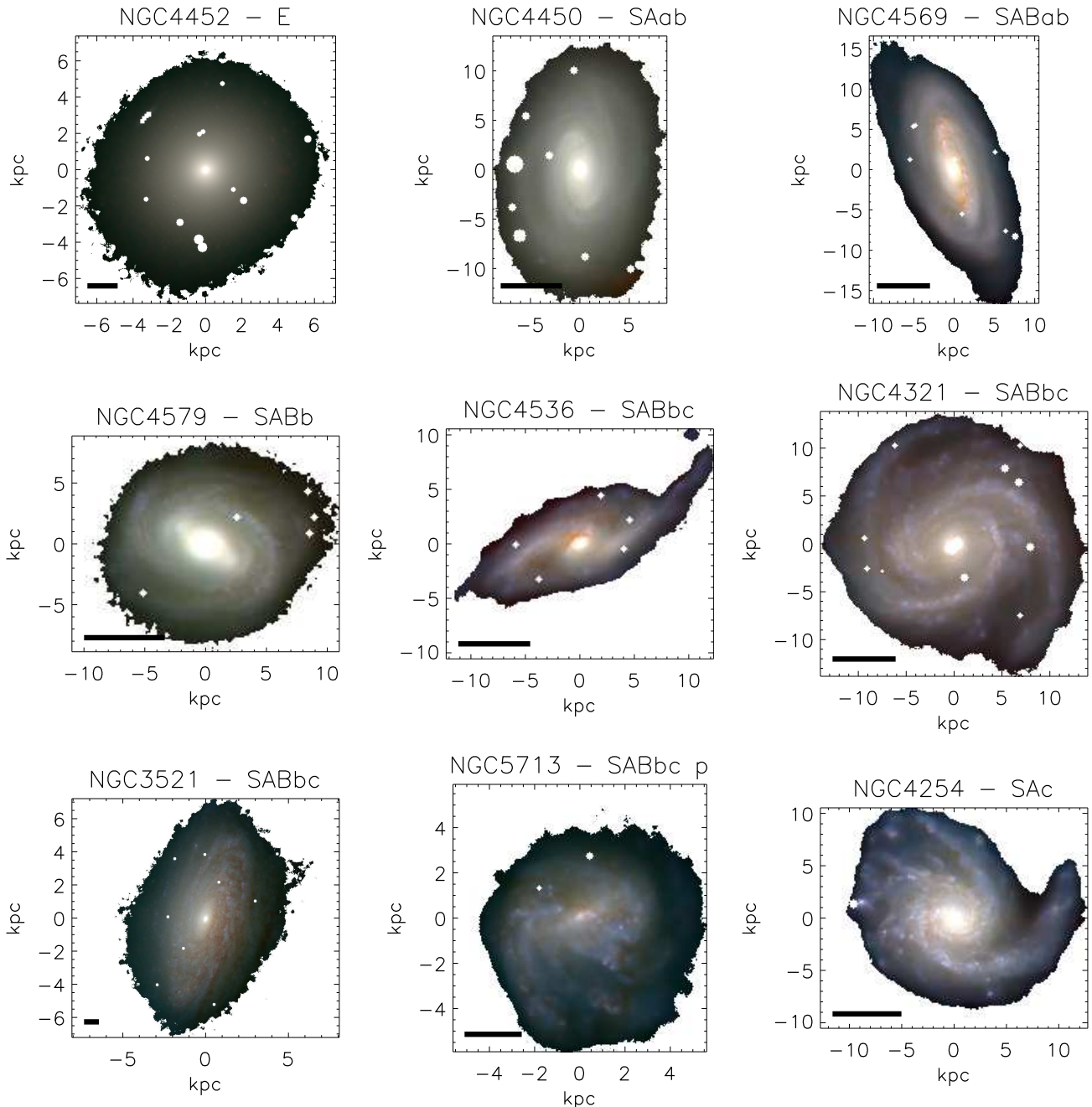


Figure 5. H (red channel) - i (green) - g (blue) colour composite image of the nine galaxies in the sample, ordered according to their Hubble type. Images are adaptively smoothed with ADAPTSMOOTH to ensure a minimum signal-to-noise ratio of 20 at each pixel and foreground stars are masked out, as explained in Section 4. Scales are in physical kpc. The black rod in each panel corresponds to 50 pixels.

regions that make it through the cut. Effectively, the intensity cut ensure that the error on colour due to background fluctuations is roughly the same as the error on the H -band only, that is 10 per cent at most.

From the adaptively smoothed and matched images in the three (or two) bands we compute colours and surface brightness in solar units per pc^2 (in the “luminance” band), for each pixel. From colours we derive the M/L ratio as explained in Sec. 2 and can multiply it by the surface brightness in order to obtain the stellar mass surface density.

4.2 Models and observations in the colour-colour space

Before illustrating the results of our stellar mass map reconstruction method, we check to which extent the models can actually reproduce the observed pixel-by-pixel colours in galaxies. In Figure 6 we plot the distribution of pixels in the $(g - i, i - H[K_s])$ space for the nine galaxies in our sample. The relative number density of pixels per colour cell is displayed according to the colour key on the right side. On the

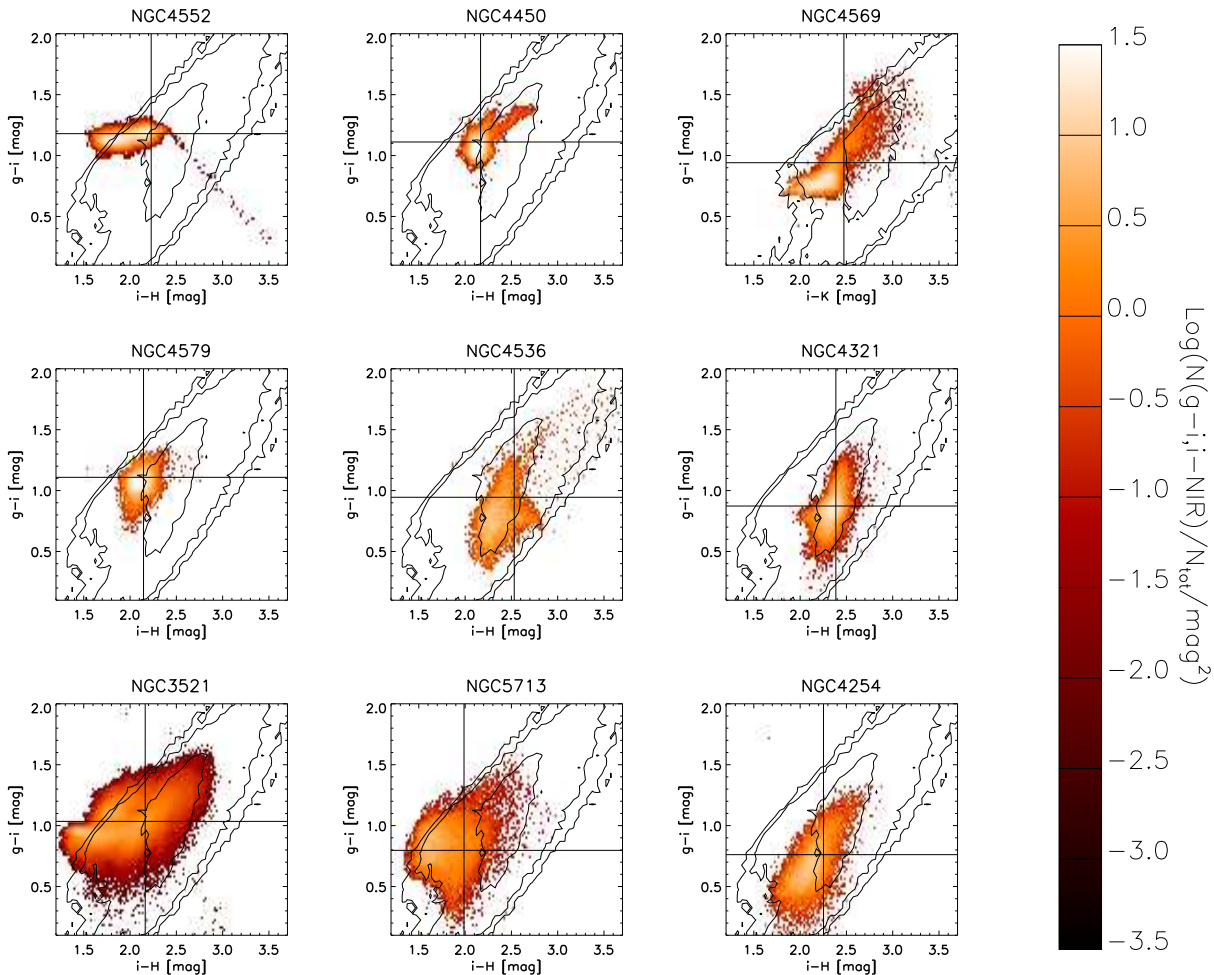


Figure 6. Distribution of pixels in the $(i-H)$ - $(g-i)$ colour-colour space, given in fraction of pixels per cell of mag^2 . Black contours represent the prior distribution of models (1, 10 and 100 models per bin) in the CB07 library. The models match the observed distributions well, with a few minor exceptions discussed in the text.

top of it we overlay contours showing the number density of models in our library. We observe that the vast majority of pixels in our galaxies lie within the contours that trace the distribution of models. Although this is *not* a proof that models are correct, it reassures us that we can reproduce the observations. On the other hand, a comparison with Figure A1 shows that broad ranges in all physical parameters are required for the models to match the observed colours.

Few pixels have colours are not covered by models, in NGC 4552, NGC 3521 and NGC 5713. Their M/L ratio must be derived via extrapolation (minimum surface curvature fitting). We have scrutinized these pixels that lie blue-ward of the model contours (in $i-H$) and found that they are from the lowest surface brightness regions. A possible explanation for this could be just the influence of background fluctuations in the NIR, that can certainly account for errors of ≈ 0.1 mag. Further, in NGC 4552 the data shows at face-value a strong $i-H$ colour gradient, with bluer values at larger radii, which does not correspond to any similar trend in $g-i$. A non-uniform background cannot explain this effect, since the strength of this gradient appears the same at different position angles. A metallicity gradient can also be

invoked, but not as a full explanation, since we do have low metallicity models in our library and yet we are unable to recover such blue $i-H$. Michard (2002) and Wu et al. (2005) have pointed out in the past that optical thinned CCDs can have very extended PSF wings (especially in i band), up to arcminute scales. Such wings are not expected in the NIR, although no studies of the phenomenon have been conducted so far. We can speculate that large-angle PSF wings from scattering in i (and g , but not in H) band cause the “blue” $i-H$ halo around NGC 4552 (and possibly the blue “halo” around NGC 3521 and 5713). Indeed, we observed the very same effect also in another elliptical of similar apparent size and luminosity, NGC 4621 (which is not in the current sample).

Despite those possible systematics at low surface brightness levels, Fig. 6 suggests that our method is on a solid footing for regions within the classically defined optical radius of a galaxy.

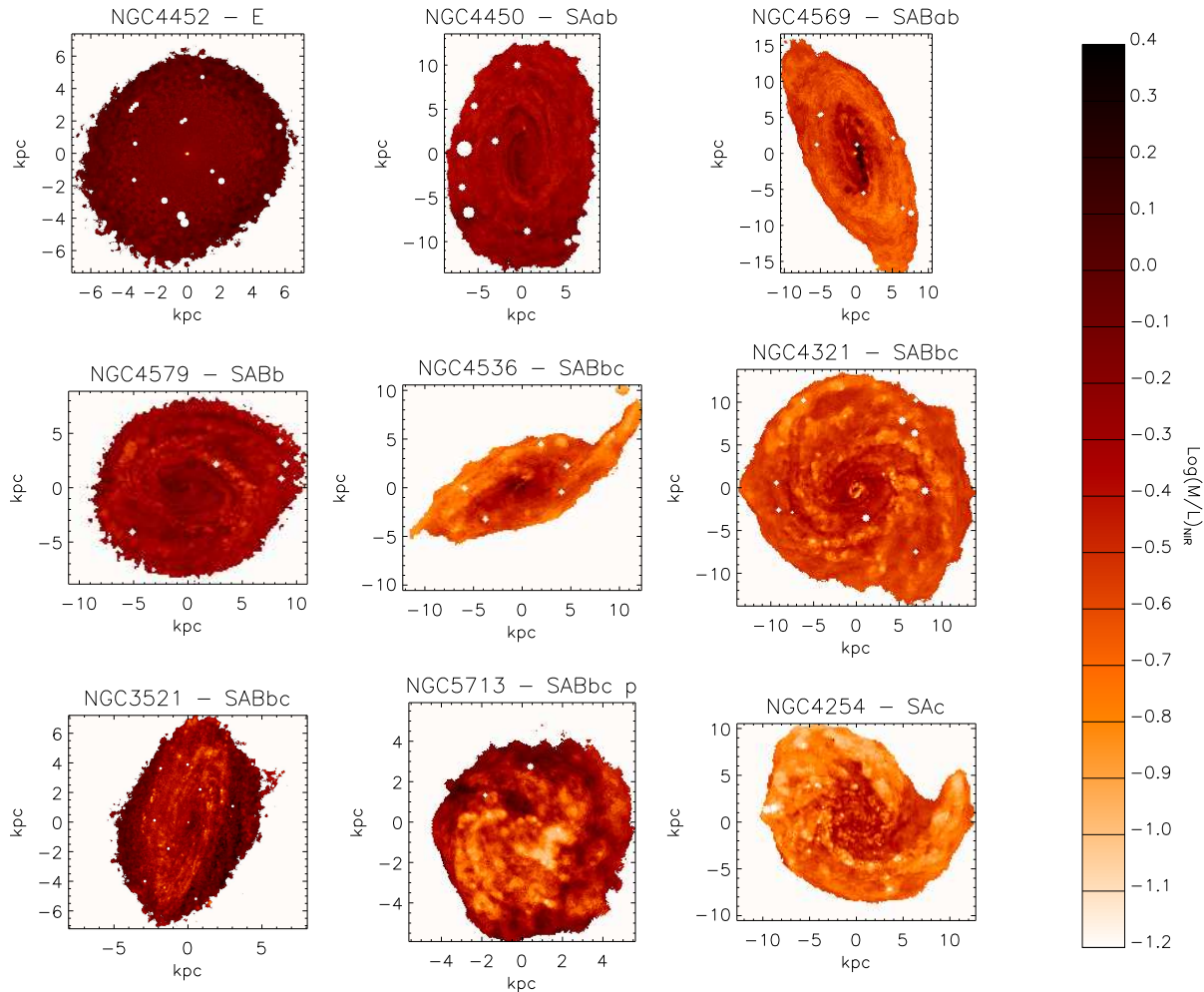


Figure 7. Maps of $\log \Upsilon_H$ for the nine galaxies.

5 RESULTS

5.1 M/L and mass maps

In Figure 7 we show the resulting M/L maps ($H[K_s]$ -band) for the nine galaxies, with light (dark) tints representing low (high) M/L , as indicated in the side colour key. Early type galaxies tend to have uniform M/L , due to their phase-mixed stellar populations and lack of substantial dust obscuration⁸. In later type galaxies young, blue stellar populations in the spiral arms result in a spiral structure of lower M/L . For the two grand-design spirals (NGC 4321 and 4254) the radial decrease of M/L is a clear effect of the younger, lower metallicity stars that populate the outer disk (see e.g. Portinari & Salucci 2009). The presence of an old/metal rich bulge is at the origin of the high- M/L regions in the inner parts of most spirals, except NGC 5713 which has a peculiar morphology. Dust lanes, which are observable in the true colour images of Fig. 5 as reddish intrusions, are highlighted

⁸ Note the bright nucleus in NGC 4452: the LINER shines in blue $g-i$ colour that is “interpreted” by our algorithm as young stellar populations. The nuclear pixels can also be seen as a track directed towards the lower-right corner in Fig. 6.

in the M/L maps by the most extreme high values, as one expects as a consequence of light absorption.

The stellar mass maps, resulting from multiplying $H[K_s]$ -band intensity with the M/L of Fig. 7, are shown in Figure 8. What is most striking here is the overall smoothness of the stellar mass distribution across the entire morphological sequence. The prominent spiral arms which are seen in the true colour images (and in the individual bands) are greatly reduced in the mass maps. We will quantitatively analyze the relative bias of galaxy structure in mass maps versus brightness maps at different wavelength in paper II of this series. To give a more quantitative idea of how structure changes from a light-weighted to a mass weighted view, we note that the relative arm-interarm contrast for NGC 4321 decreases roughly by a factor 2 when we measure it from the mass map rather than from i or H band images.

5.2 Comparison between different methods

We now compare the stellar mass maps obtained with the different methods described in paragraph 2. We consider (a) our fiducial method based on $\Upsilon_H(i-H, g-i)$ as derived from CB07 SPS models, in conjunction with H -band images; (b) $\Upsilon_H(i-H, g-i)$ from BC03 SPS models, with H -band im-

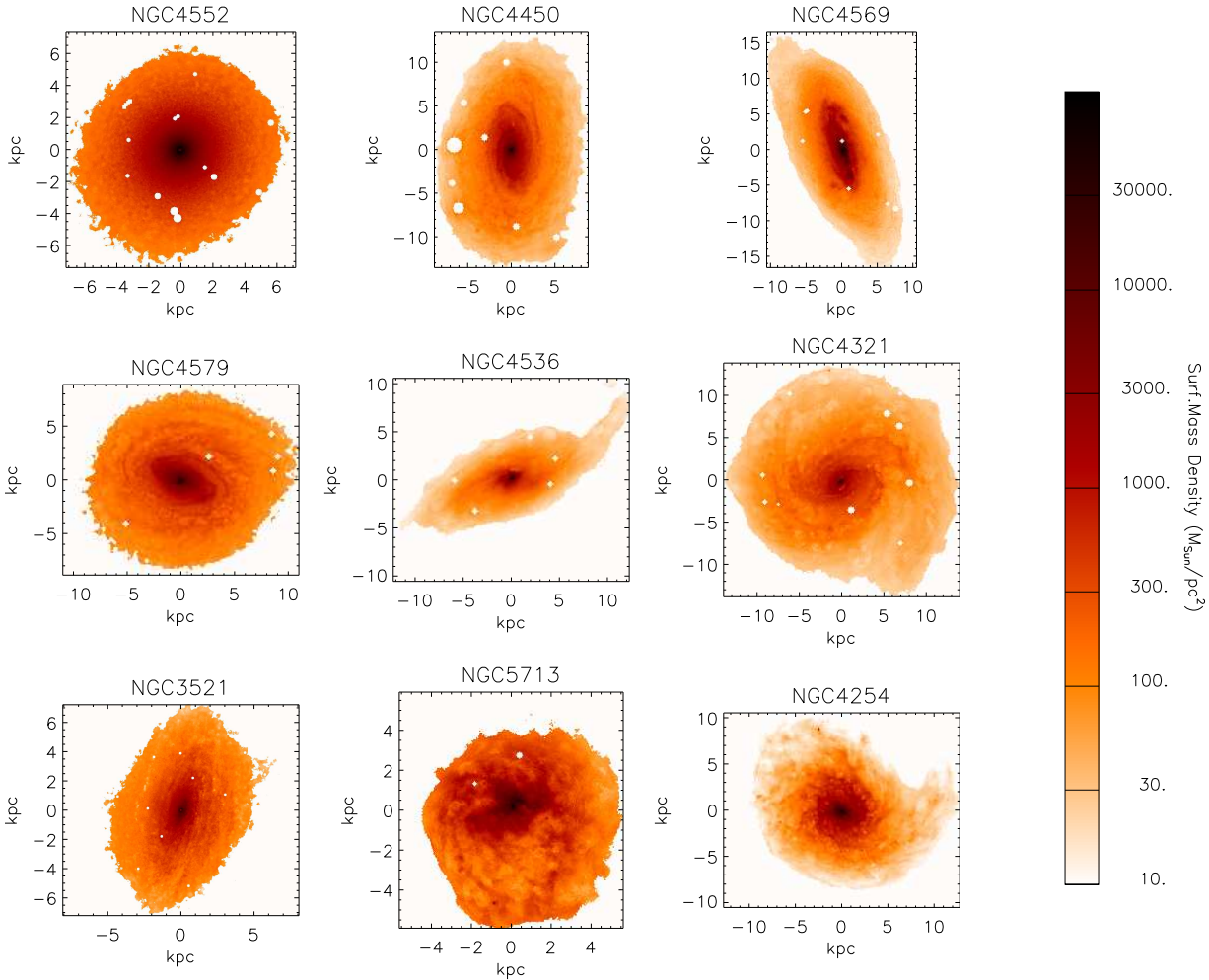


Figure 8. Stellar mass surface density maps for the nine galaxies.

ages; (c) $\Upsilon_H(g-i)$ from CB07 SPS models, with H -band images; (d) $\Upsilon_i(g-i)$ from CB07 SPS models, in conjunction with the i -band images. In particular, we present such comparisons for NGC 4321, which is representative of normal galaxies with minor dusty regions and moderate star formation activity, and for NGC 5713, which is the extreme case in terms of dusty and intensely star forming regions. Mass maps comparisons for NGC 4321 and 5713 are presented in Figures 9 and 10, respectively. In both figures, the top left panel shows the stellar mass map obtained with the fiducial method (a). The other three panels display the logarithmic difference between the mass maps obtained with methods (b), (c) and (d), respectively, and that from the fiducial method (a). For NGC 4321 we observe that the four methods result in very similar structure, with $r.m.s.$ in the residuals between 5 and 7 per cent. Method (d) ($\Upsilon_i(g-i)$ from CB07) provides the closest match to the default method (a), with an average pixel-by-pixel offset of 3 per cent and residual $r.m.s.$ of 5 per cent. Using $g-i$ alone to constrain M/L in H band results in worse agreement with method (a) ($r.m.s. = 7$ per cent). This is expected from Fig. 1 and 4: while Υ_i shows little dependence on $i-H$, on the contrary Υ_H does significantly depend on both colours. As for the difference between using CB07 or BC03 (method a and b), we note a systematic

offset of approximately $+0.1$ dex going from CB07 to BC03, although the difference map looks very uniform.

Contrary to the “normal” galaxy NGC 4321, NGC 5713 is characterized by intensely star forming regions and prominent dust lanes. Models based on CB07 and BC03 predict very different M/L especially in presence of very young stellar populations (see Fig. 3), as shown in the top-right panel of Fig. 10. All blue regions (cf. Fig. 5) have masses over-estimated by up to 0.4 dex (2.5 times) in BC03 models. A qualitatively similar (but quantitatively smaller, up to 0.25 dex only) over-estimate of the mass of regions dominated by young stellar populations arises from method (d): in this case the median $\Upsilon_i(g-i)$ is not representative for these extreme stellar populations that lie to the leftmost edge of the model colour distribution (see Fig. 6). This appears to be the case also for method (c) and demonstrates the need for a second colour to properly describe this region of the parameter space.

We further explore the relative bias of different stellar mass estimation methods in Figure 11. We consider the total stellar mass of galaxies as given by the integral of the resolved maps and plot the logarithmic difference with respect to our reference method (a). In addition to the four methods discussed above we show the relative bias for other three

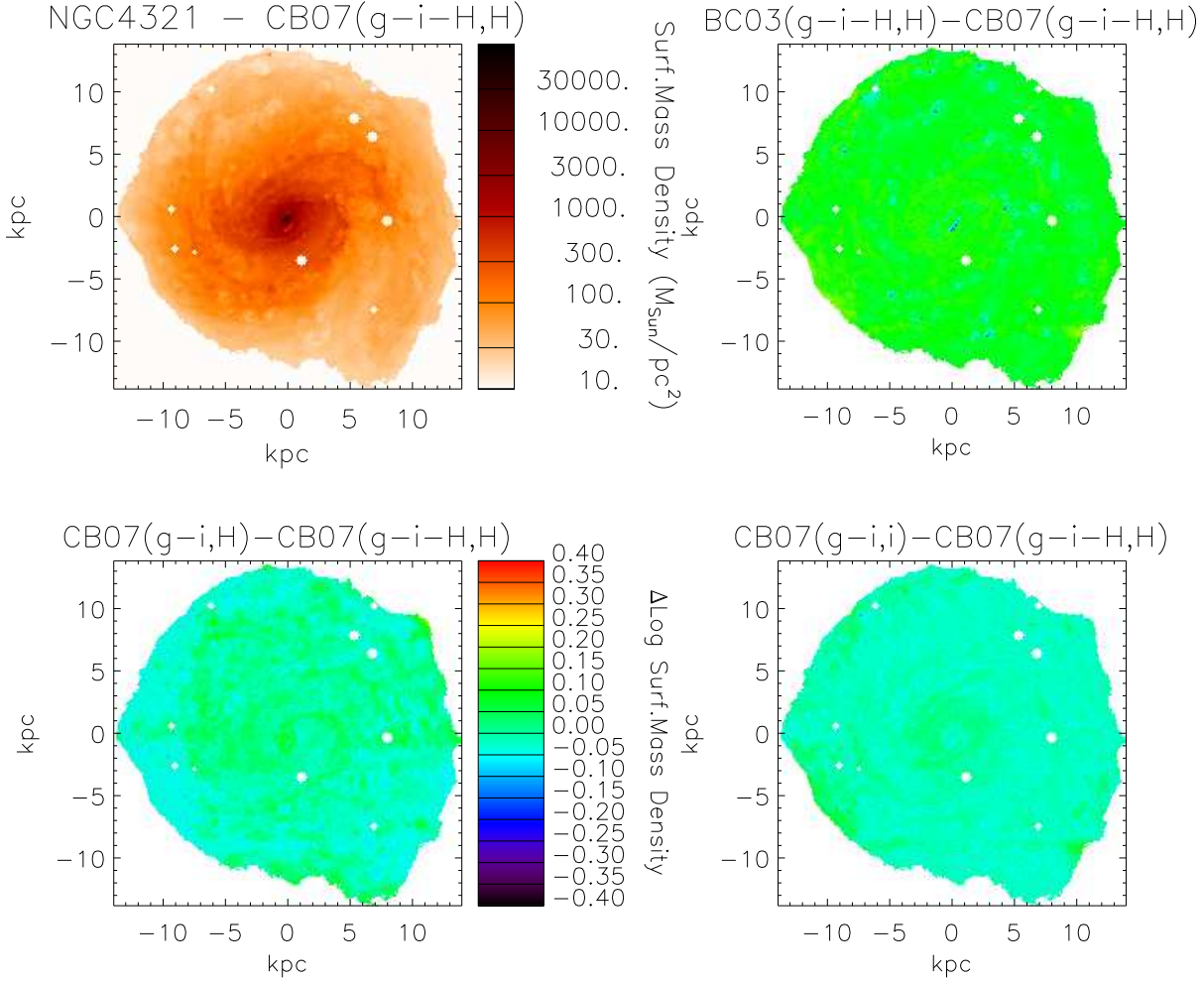


Figure 9. Comparison between stellar mass maps obtained with different methods/models for NGC4321 (M100). *Top left panel* is the map obtained with our fiducial model CB07 using two colours ($i-H$), ($g-i$) to extract M/L in H -band. The other three panels show the logarithmic difference between three alternative methods and the fiducial one. In the *top right panel* we use the same method applied to BC03 models. In the *bottom left panel* we use CB07 again, but Υ_H is derived from $g-i$ alone (see Fig. 1, top left panel). Finally, in the *bottom right panel* M/L is determined in i band from $g-i$ alone (see Fig. 4 left panel) from CB07 models.

methods: $\Upsilon_i(g-i)$ based on BC03 models, $\Upsilon_H(g-i)$ and $\Upsilon_i(g-i)$ based on Bell et al. (2003) fitting formulae. Galaxies are sorted in morphological type, from E to the left to Sc to the right, and different symbols refer to different methods, according to the figure legend. We observe that total mass estimates from $\Upsilon_i(g-i)$ (CB07) is in excellent agreement with our fiducial method $\Upsilon_H(g-i, i-H)$ (CB07): absolute deviations are < 0.03 dex for all galaxies (0.012 dex on average) and no bias is seen ($< \Delta \log M_* \geq -0.004$ dex). As already noted on the resolved maps of Figures 9 and 10, using the optical $g-i$ colour index alone to constrain M/L in NIR bands provides instead a very poor match to the results of the 2-colour method: mass estimates are biased low by approximately 0.1 dex for most galaxies and a substantial scatter is seen.

Mass estimates based on BC03 models give systematically higher values with respect to CB07: this is not surprising given the lower M/L in CB07 due to the new TP-AGB prescription and is consistent with Figure 8 of Cimatti et al.

(2008). However, by comparing stellar mass estimates based on BC03 model predictions we note that those based on H -band are systematically higher than those based on i -band, as opposed to the absence of bias observed with CB07 models. This might be an indication that the role of TP-AGB stars in BC03 models is under-estimated: in fact, the emission of these stars is relatively more intense in H than in i band; hence, by under-estimating their contribution one would conversely over-estimate M/L by a larger amount in H than in i band.

Mass estimates based on the fitting formulae of Bell et al. (2003) are substantially higher than all mass estimates based on our models, as expected from Fig. 3 and 4. In particular, using these fitting formulae we grossly over-estimates the stellar masses of blue star-forming galaxies, up to by a factor 2.5. We stress that the difference cannot be due to the new TP-AGB prescription alone: the Bell et al. (2003) formulae rely on BC03 SPS models, yet they over-estimates stellar masses even relative to our BC03-based

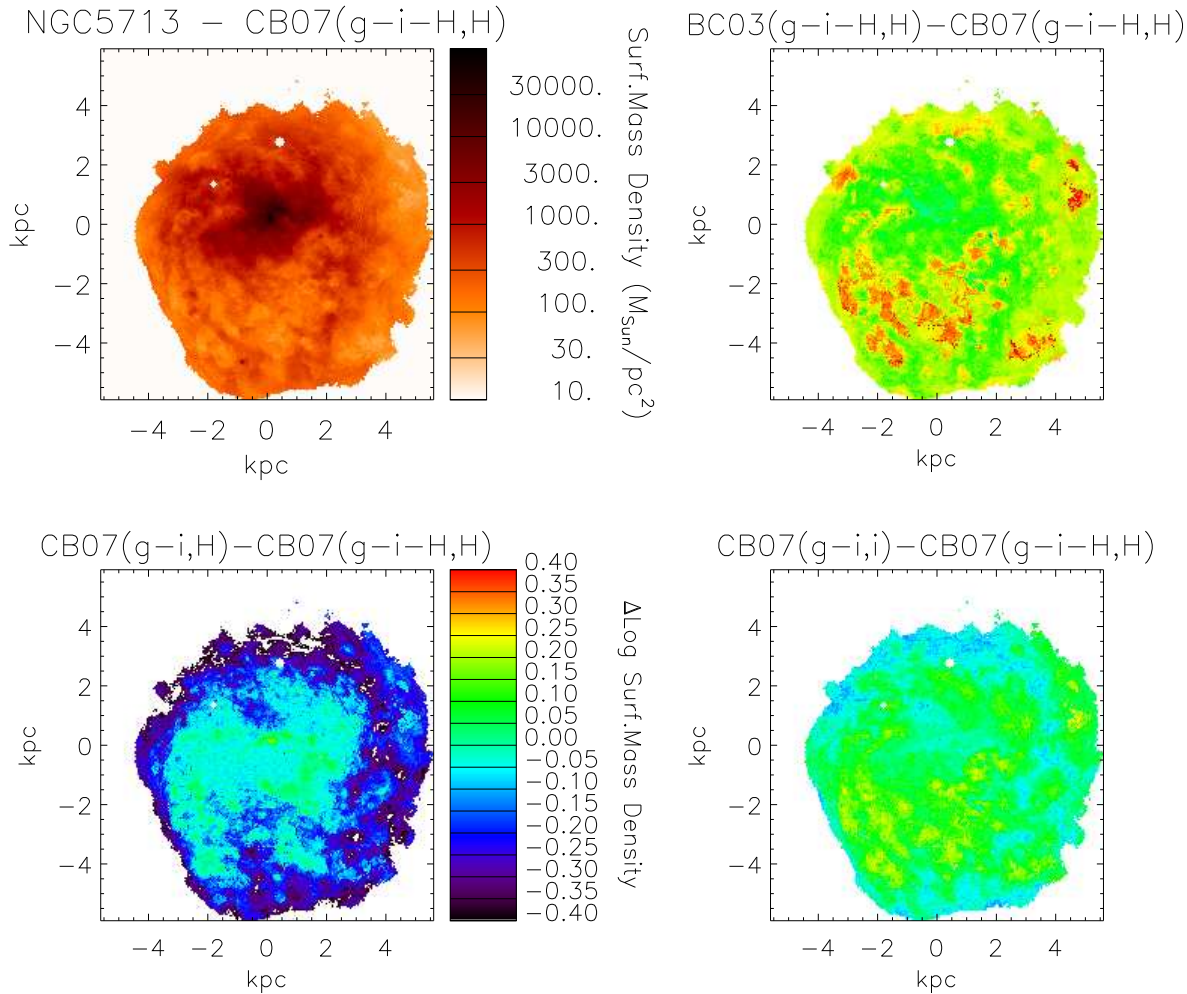


Figure 10. Same as Fig. 9 but for NGC5713.

methods. As discussed in section 2, the main reason why our estimates differ from Bell et al.’s is the different prior distribution of star formation histories, particularly concerning the age and the relative importance of bursts. Despite the smaller dynamical range of M/L in Bell et al.’s models, mass estimates derived from their prescription based on i and H band respectively are in reasonable agreement only for 6/9 galaxies; in the other three cases they disagree by approximately 0.15 dex (40 per cent). This indicates that Bell et al.’s fitting formulae have, in general, a poor internal consistency if applied pixel by pixel.

5.3 Mass estimates from colour maps vs. global colours

In this section we investigate the difference in determining the total stellar mass of a galaxy by integrating resolved stellar mass maps, like those presented in the previous sections, and by using global fluxes and colours to estimate M/L , as is usually done. More specifically, we are going to compare

$$M_{*,\text{resolved}} = \sum_j f_{H,j} \Upsilon_H[(g-i)_j, (i-H)_j] \quad (2)$$

against

$$M_{*,\text{unresolved}} = \Upsilon_H[(g-i)_{\text{global}}, (i-H)_{\text{global}}] \sum_j f_{H,j} \quad (3)$$

where f_H is the H -band surface brightness and the index j denotes quantities for individual pixels. We call Q the ratio $\frac{M_{*,\text{unresolved}}}{M_{*,\text{resolved}}}$ and report this number for each galaxy in the nine panels of Fig. 12. For 4 of 9 galaxies the ratio Q is close to 1 within a few per cent, but for the others $Q < 0.9$ down to 0.6. This indicates that the same mass estimator drawing on global colours misses 40 per cent of the mass measured in a resolved map. The source of this difference is illustrated by the histograms of Fig. 12 and ultimately can be traced to the strong non-linearity of the relation between colour(s) and M/L . For each galaxy all pixels are binned according to their estimated *local* Υ_H . The gray-shaded histogram represents the mass in each bin as computed from the local flux and Υ_H . The empty histogram shows the mass contributed by each bin if Υ_H from total fluxes (marked by the vertical dot-dashed line) were adopted. As obvious, the grey histogram is above the empty histogram for all bins where Υ_H is larger than the global value and, conversely, it

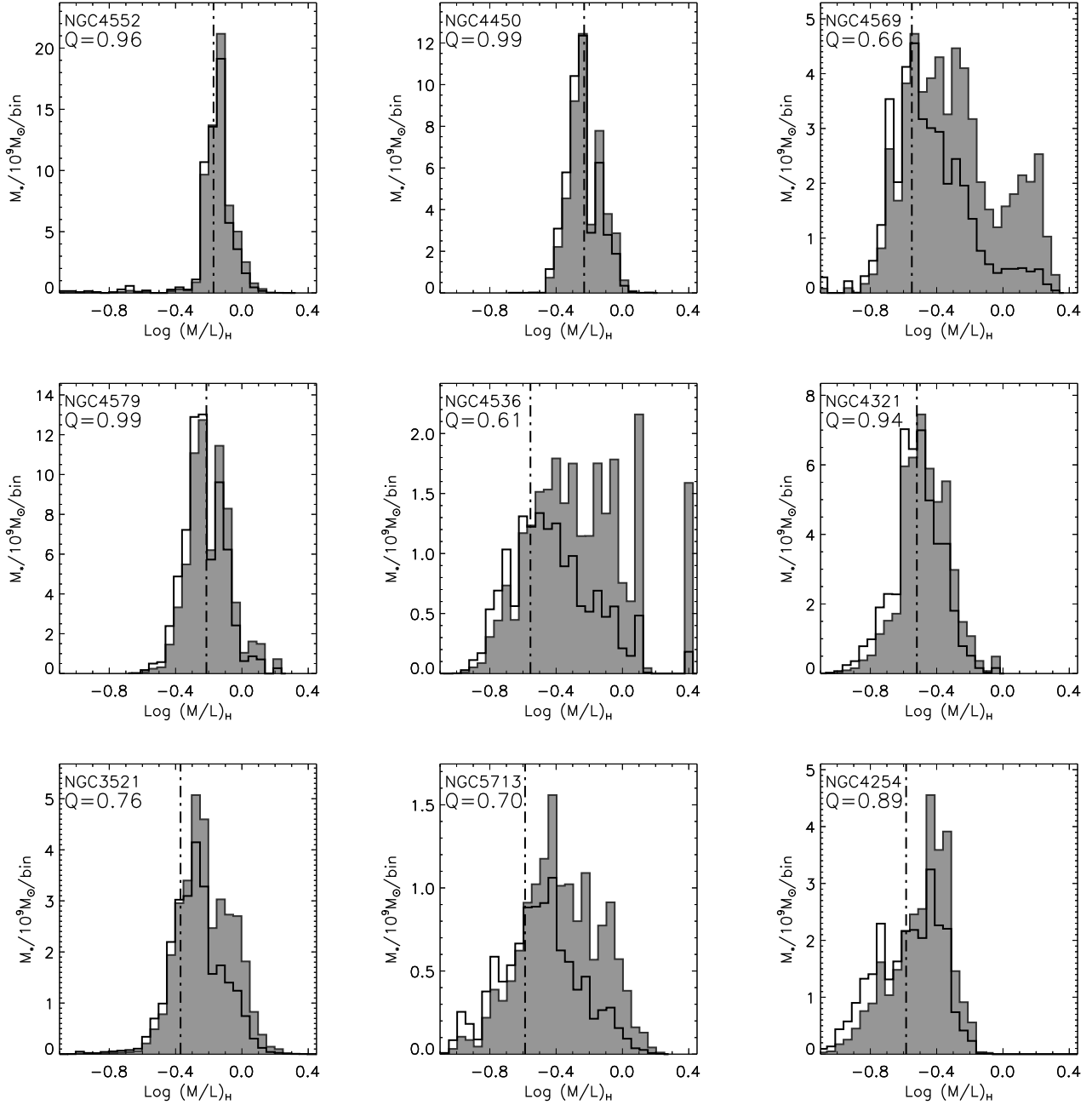


Figure 12. Distributions of stellar mass computed using the proper local Υ_H (grey histogram) and the global Υ_H as derived from global colours (empty histogram), as a function of *local* Υ_H . The dot-dashed line marks the global Υ_H . The ratio Q between total stellar mass estimated drawing on unresolved and on resolved photometry is also reported in each panel.

is below for bins where Υ_H is smaller. The area below the grey histogram gives the stellar mass estimate from resolved mass maps, while the area below the empty histogram gives the mass based on global colours. For narrow Υ_H distributions the difference between the pixels where the global M/L overestimates the mass and those where it underestimates it almost balances: this is the case for NGC4552, NGC4450, NGC4579, NGC4321, that all have $Q > 0.9$. For broader distributions in Υ_H we observe two facts: *i*) the global M/L is lower than the mean of the distribution, because low Υ_H regions dominate the flux and hence the colours of the galaxy;

ii) the extended high Υ_H wing is exponentially amplified in the grey histogram with respect to the empty one. As a result, galaxies with a broad M/L distribution have large differences between resolved and unresolved mass estimates, up to approximately 40 per cent. As we can see comparing Fig. 12 and 5, this is especially the case for galaxies with substantive dust-obscured regions (i.e. NGC4569, NGC4536, NGC3521 and NGC5713). Dust obscured regions, in fact, contribute a minor fraction of the flux and influence the global colours only marginally, although they may conceal a significant amount of stellar mass. In our most extreme case,

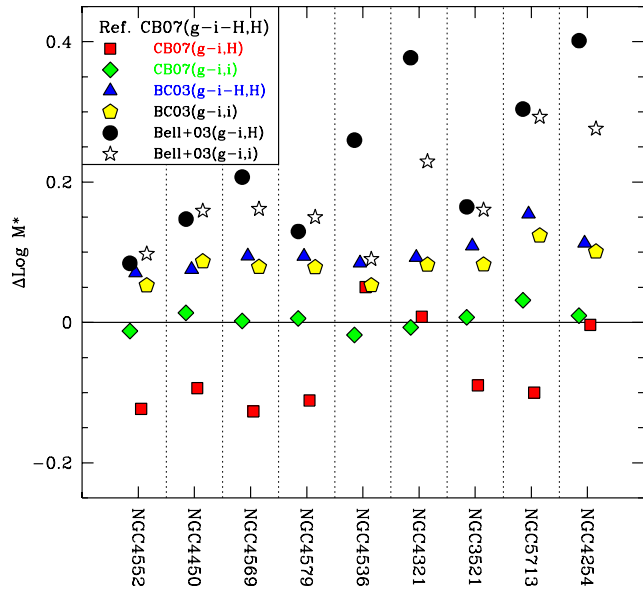


Figure 11. Comparison between total stellar masses from resolved maps derived using different methods and/or models. For each galaxy the logarithmic difference with respect to our fiducial method is plotted. Different symbols correspond to different methods/models, as indicated in the legend.

NGC 4536, regions with $\Upsilon_H > 1$ contribute only roughly 7 per cent of the total H -band luminosity, but around 20 per cent of the stellar mass. Such a low impact in terms of luminosity also implies that these dust obscured regions can affect the global colours at a level of ≈ 0.1 mag at most, such that it is *observationally* impossible to correctly weight them using *unresolved* photometry.

In Fig. 13 we analyze the difference between unresolved and resolved total stellar mass estimates for different methods, as indicated in the legend. We plot the logarithmic difference between unresolved and resolved total stellar mass estimates (i.e. $\log Q$) both obtained with the same method. The dustiest and most irregular galaxies (namely, NGC 4569, NGC 4536, NGC 3521, NGC 5713) display the largest differences. They appear enhanced in two-colour based methods, most likely because these methods can better disentangle between dust and other stellar population parameters. For the other five more regular galaxies a clear trend is observable for all methods: the differences between resolved and unresolved stellar mass estimates increase going from early to late types. This is just a consequence of mass differences being larger for larger pixel colour spread and of colour spread being larger in later type galaxies (i.e. of early type galaxies being more uniform).

The dynamical range of models in M/L determines the relative amplitude of the unresolved estimate bias. For a given model library and method (one or two colours), this is generally smaller in the NIR than in i band. The bias is also smaller using Bell et al.’s fitting formulae, which have a much smaller M/L dynamical range with respect to our model libraries.

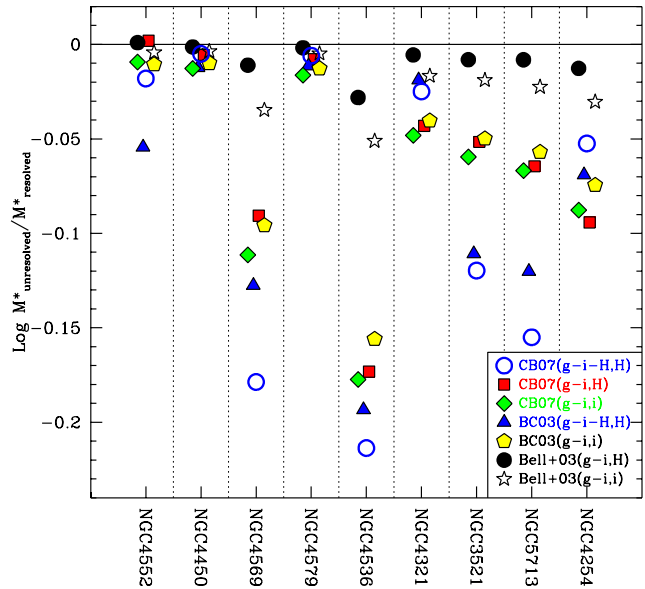


Figure 13. Logarithmic differences between total stellar mass estimates obtained from unresolved photometry and by integrating resolved maps, both based on the *same* method/models. Different methods/models are shown with different symbols, as shown in the legend.

In Section 2.4 we argued that our model libraries are better suited to describe local scales in terms of SFH and dust attenuation with respect to the Bell et al. (2003) fitting formulae. However we left the question open whether Bell et al. (2003) might provide better fits to the SED of galaxies as a whole, as they are less biased toward star formation bursts. If this is the case, we must expect Bell et al.’s stellar mass estimates based on unresolved photometry to agree with our own estimates from resolved maps better than our estimates based on unresolved photometry do. In order to make this comparison fair in terms of SPS models, we confront the estimates based on Bell et al.’s formulae with our BC03-based ones. We find that mass estimates based on Bell et al.’s $\Upsilon_H(g-i)$ and unresolved photometry are on average 0.12 dex larger than estimates done by integrating mass maps based on BC03 $\Upsilon_H(i-H, g-i)$ (*r.m.s.* 0.1 dex), whereas masses derived with BC03 $\Upsilon_H(i-H, g-i)$ drawing on unresolved photometry are smaller by 0.08 dex on average (*r.m.s.* 0.06 dex). This shows that even with unresolved photometry (and assuming the same SPS models) Bell et al. (2003)’s fitting formulae do not perform better than our look-up tables do.

6 SUMMARY AND CONCLUDING REMARKS

In this paper we have developed a method that is capable of reconstructing resolved stellar mass maps of galaxies from multi-band optical/NIR imaging, with typical statistical uncertainties of 0.1 – 0.15 dex on local scales. We have realized a Monte Carlo spectral library of synthetic stellar populations based on the 2007 version of Bruzual & Charlot

(2003) code (CB07), which includes a new prescription to treat the TP-AGB stellar evolutionary phase according to the latest isochrones by Marigo & Girardi (2007) and Marigo et al. (2008). Prescriptions to treat dust à la Charlot & Fall (2000) are also incorporated. By marginalizing over all other parameters we obtain look-up tables that contain median estimates of M/L in different bands as a function of one or two optical/NIR colours.

From practical and theoretical considerations we arrive at g , i and $H[K_s]$ as a good set of band-passes and express $\Sigma_{M*} = \Sigma_H \Upsilon_H(g - i, i - H)$: this combination allows to carefully take young stellar populations and dust obscuration into account, while avoiding strong $H\alpha$ contamination in HII regions. We demonstrated that the use of a second colour is required to determine Υ_H with uncertainties as low as 0.1 – 0.15 dex. Combining g and i bands alone, $\Sigma_{M*} = \Sigma_i \Upsilon_i(g - i)$, provides a good approximation to our best method based on g , i , H for “normal”, close to face-on galaxies. However it may give highly biased results in presence of very young stellar populations or severe dust extinction, where the i band flux (7000 Å) is much more sub-dominant, in the first case, or more attenuated than in NIR (1 – 2 μm), in the second case.

On the other hand, the flux in the NIR bands appears more sensitive to the still debated role of TP-AGB stars: old models with shorter-lived TP-AGB stars over-estimate M/L ratios in H -band by ≈ 0.1 dex (even up to 0.4 dex for young, unextincted stellar populations) with respect to the current models.

It must be stressed that we account for dust only through its 4π -averaged extinction (see Charlot & Fall 2000). Although this assumption is generally reasonable, there are cases where it fails, such as NGC 3521 (Fig. 5): it is immediate to see that the far part of the dusty disk (on the East side) reflects back the light of the bright inner regions of the small bulge and the disk. This results in the artificial asymmetry of the reconstructed mass map of Fig. 8. This kind of artifacts are unavoidable unless a very careful 3D radiative transfer modeling is performed, which is well beyond the scope of the present mass reconstruction method.

We have applied our modeling to a small pilot sample of nearby galaxies, creating pixel-by-pixel maps of the stellar surface mass density. In general, these maps look quite smooth (Fig. 8), and hence dynamically plausible, with the prominent spiral arms of young stars and dust greatly reduced. Detailed comparisons with estimates of dynamical disc mass via vertical kinematics will enable us to accurately quantify systematics in our method. We note that preliminary results⁹ from the DiskMass survey (Verheijen et al. 2007) appear in good agreement with the M/L ratios inferred in this work, which are significantly lower than those derived using the prescriptions of Bell et al. (2003).

Our analysis highlights an important bias in total stellar mass estimates when spatially unresolved photometric measurements and colours are used: the stellar mass contribution of dust obscured regions to the total is severely underestimated from unresolved photometry, as those regions

contribute very little flux and negligibly affect colours. Mass estimates based on global fluxes can be biased low by up to 40 per cent. The present sample is too small to draw conclusions on the consequences that this effect may have for galaxy stellar mass functions, but we can envisage that resolved mass estimates may steepen the faint-end slope of the stellar mass functions as estimated so far. We will address this issue with a larger and more representative sample in a forthcoming paper of this series.

After having put the foundations to obtain stellar mass maps in this paper, in the following papers of this series we will address questions like: how do structural parameters change going from light to stellar mass? How can we quantify the bias in unresolved stellar mass estimates as a function of other observational parameters? How do SED properties depend on local stellar mass surface density? Can the inclusion of constraints from longer wavelength improve our mass reconstruction method?

ACKNOWLEDGMENTS

We thank Peppo Gavazzi for giving seminal motivation to this work. We are also thankful to Simon White, Eric Bell, Anna Gallazzi, Matt Bershady, Kelly Foyle, Elisabete Da Cunha and Paolo Salucci for useful discussions and comments.

This research has made use of the GOLD Mine Database (<http://goldmine.mib.infn.it>).

This work was funded in part by the Marie Curie Initial Training Network ELIXIR of the European Commission under contract PITN-GA-2008-214227.

Funding for the SDSS and SDSS-II has been provided by the Alfred P. Sloan Foundation, the Participating Institutions, the National Science Foundation, the U.S. Department of Energy, the National Aeronautics and Space Administration, the Japanese Monbukagakusho, the Max Planck Society, and the Higher Education Funding Council for England. The SDSS Web Site is <http://www.sdss.org/>.

The SDSS is managed by the Astrophysical Research Consortium for the Participating Institutions. The Participating Institutions are the American Museum of Natural History, Astrophysical Institute Potsdam, University of Basel, University of Cambridge, Case Western Reserve University, University of Chicago, Drexel University, Fermilab, the Institute for Advanced Study, the Japan Participation Group, Johns Hopkins University, the Joint Institute for Nuclear Astrophysics, the Kavli Institute for Particle Astrophysics and Cosmology, the Korean Scientist Group, the Chinese Academy of Sciences (LAMOST), Los Alamos National Laboratory, the Max-Planck-Institute for Astronomy (MPIA), the Max-Planck-Institute for Astrophysics (MPA), New Mexico State University, Ohio State University, University of Pittsburgh, University of Portsmouth, Princeton University, the United States Naval Observatory, and the University of Washington.

This research has made use of the NASA/IPAC Extragalactic Database (NED) which is operated by the Jet Propulsion Laboratory, California Institute of Technology, under contract with the National Aeronautics and Space Administration.

⁹ M. Bershady’s communication in “Unveiling the mass” workshop, Queen’s University, Kingston, Canada, 15-19 June, 2009.

REFERENCES

- Abraham R. G., Ellis R. S., Fabian A. C., Tanvir N. R., Glazebrook K., 1999, *MNRAS*, 303, 641
- Bell E. F., de Jong R. S., 2000, *MNRAS*, 312, 497
- Bell E. F., de Jong R. S., 2001, *ApJ*, 550, 212
- Bell E. F., McIntosh D. H., Katz N., Weinberg M. D., 2003, *ApJS*, 149, 289
- Bruzual G., 2007, in Vallenari A., Tantalò R., Portinari L., Moretti A., eds, *From Stars to Galaxies: Building the Pieces to Build Up the Universe* Vol. 374 of *Astronomical Society of the Pacific Conference Series*, *Stellar Populations: High Spectral Resolution Libraries. Improved TP-AGB Treatment*. pp 303–+
- Bruzual G., Charlot S., 2003, *MNRAS*, 344, 1000
- Casali M., et al. 2007, *A&A*, 467, 777
- Chabrier G., 2003, *ApJ*, 586, L133
- Charlot S., Fall S. M., 2000, *ApJ*, 539, 718
- Cimatti A., Cassata P., Pozzetti L., Kurk J., Mignoli M., Renzini A., Daddi E., Bolzonella M., Brusa M., Rodighiero G., Dickinson M., Franceschini A., Zamorani G., Berta S., Rosati P., Halliday C., 2008, *A&A*, 482, 21
- Conti A., Connolly A. J., Hopkins A. M., Budavári T., Szalay A. S., Csabai I., Schmidt S. J., Adams C., Petrovic N., 2003, *AJ*, 126, 2330
- da Cunha E., Charlot S., Elbaz D., 2008, *MNRAS*, 388, 1595
- de Vaucouleurs G., de Vaucouleurs A., Corwin Jr. H. G., Buta R. J., Paturel G., Fouque P., 1991, *Third Reference Catalogue of Bright Galaxies. Volume 1-3, XII*, 2069 pp. 7 figs.. Springer-Verlag Berlin Heidelberg New York
- Elmegreen D. M., Elmegreen B. G., 1984, *ApJS*, 54, 127
- Fukugita M., Ichikawa T., Gunn J. E., Doi M., Shimasaku K., Schneider D. P., 1996, *AJ*, 111, 1748
- Gallazzi A., Brinchmann J., Charlot S., White S. D. M., 2008, *MNRAS*, 383, 1439
- Gallazzi A., Charlot S., Brinchmann J., White S. D. M., Tremonti C. A., 2005, *MNRAS*, 362, 41
- Gavazzi G., Boselli A., Donati A., Franzetti P., Scodreggio M., 2003, *A&A*, 400, 451
- Gavazzi G., Boselli A., Scodreggio M., Pierini D., Belsole E., 1999, *MNRAS*, 304, 595
- Gavazzi G., Pierini D., Boselli A., 1996, *A&A*, 312, 397
- Gavazzi G., Scodreggio M., 1996, *A&A*, 312, L29
- Grosbøl P., Patsis P. A., Pompei E., 2004, *A&A*, 423, 849
- Gunn J. E., et al. 1998, *AJ*, 116, 3040
- Gunn J. E., et al. 2006, *AJ*, 131, 2332
- Hambly N. C., Collins R. S., Cross N. J. G., Mann R. G., Read M. A., Sutorius E. T. W., Bond I., Bryant J., Emerson J. P., Lawrence A., Rimoldini L., Stewart J. M., Williams P. M., Adamson A., Hirst P., Dye S., Warren S. J., 2008, *MNRAS*, 384, 637
- Hewett P. C., Warren S. J., Leggett S. K., Hodgkin S. T., 2006, *MNRAS*, 367, 454
- Hodgkin S. T., Irwin M. J., Hewett P. C., Warren S. J., 2008, *ArXiv e-prints*
- Jarrett T. H., Chester T., Cutri R., Schneider S., Skrutskie M., Huchra J. P., 2000, *AJ*, 119, 2498
- Kauffmann G., et al. 2003, *MNRAS*, 341, 33
- Kauffmann G., Heckman T. M., White S. D. M., Charlot S., Tremonti C., Peng E. W., Seibert M., Brinkmann J., Nichol R. C., SubbaRao M., York D., 2003, *MNRAS*, 341, 54
- Kendall S., Kennicutt R. C., Clarke C., Thornley M. D., 2008, *MNRAS*, 387, 1007
- Kennicutt Jr. R. C., et al. 2003, *PASP*, 115, 928
- Kong X., Charlot S., Brinchmann J., Fall S. M., 2004, *MNRAS*, 349, 769
- Lawrence A., et al. 2007, *MNRAS*, 379, 1599
- Maraston C., 2005, *MNRAS*, 362, 799
- Marigo P., Girardi L., 2007, *A&A*, 469, 239
- Marigo P., Girardi L., Bressan A., Groenewegen M. A. T., Silva L., Granato G. L., 2008, *A&A*, 482, 883
- Michard R., 2002, *A&A*, 384, 763
- Portinari L., Salucci P., 2009, *ArXiv e-prints*
- Rix H.-W., Zaritsky D., 1995, *ApJ*, 447, 82
- Schlegel D. J., Finkbeiner D. P., Davis M., 1998, *ApJ*, 500, 525
- Scodreggio M., Gavazzi G., Franzetti P., Boselli A., Zibetti S., Pierini D., 2002, *A&A*, 384, 812
- Seigar M. S., James P. A., 1998, *MNRAS*, 299, 685
- Smith J. A., et al. 2002, *AJ*, 123, 2121
- Tremonti C. A., Heckman T. M., Kauffmann G., Brinchmann J., Charlot S., White S. D. M., Seibert M., Peng E. W., Schlegel D. J., Uomoto A., Fukugita M., Brinkmann J., 2004, *ApJ*, 613, 898
- van den Bosch F. C., Pasquali A., Yang X., Mo H. J., Weinmann S., McIntosh D. H., Aquino D., 2008, *ArXiv e-prints*
- Verheijen M. A. W., Bershady M. A., Swaters R. A., Andersen D. R., Westfall K. B., 2007, in de Jong R. S. editor, *Island Universes - Structure and Evolution of Disk Galaxies: The Disk Mass Project* pp 95–+
- Wu H., Shao Z., Mo H. J., Xia X., Deng Z., 2005, *ApJ*, 622, 244
- York D. G., et al. 2000, *AJ*, 120, 1579

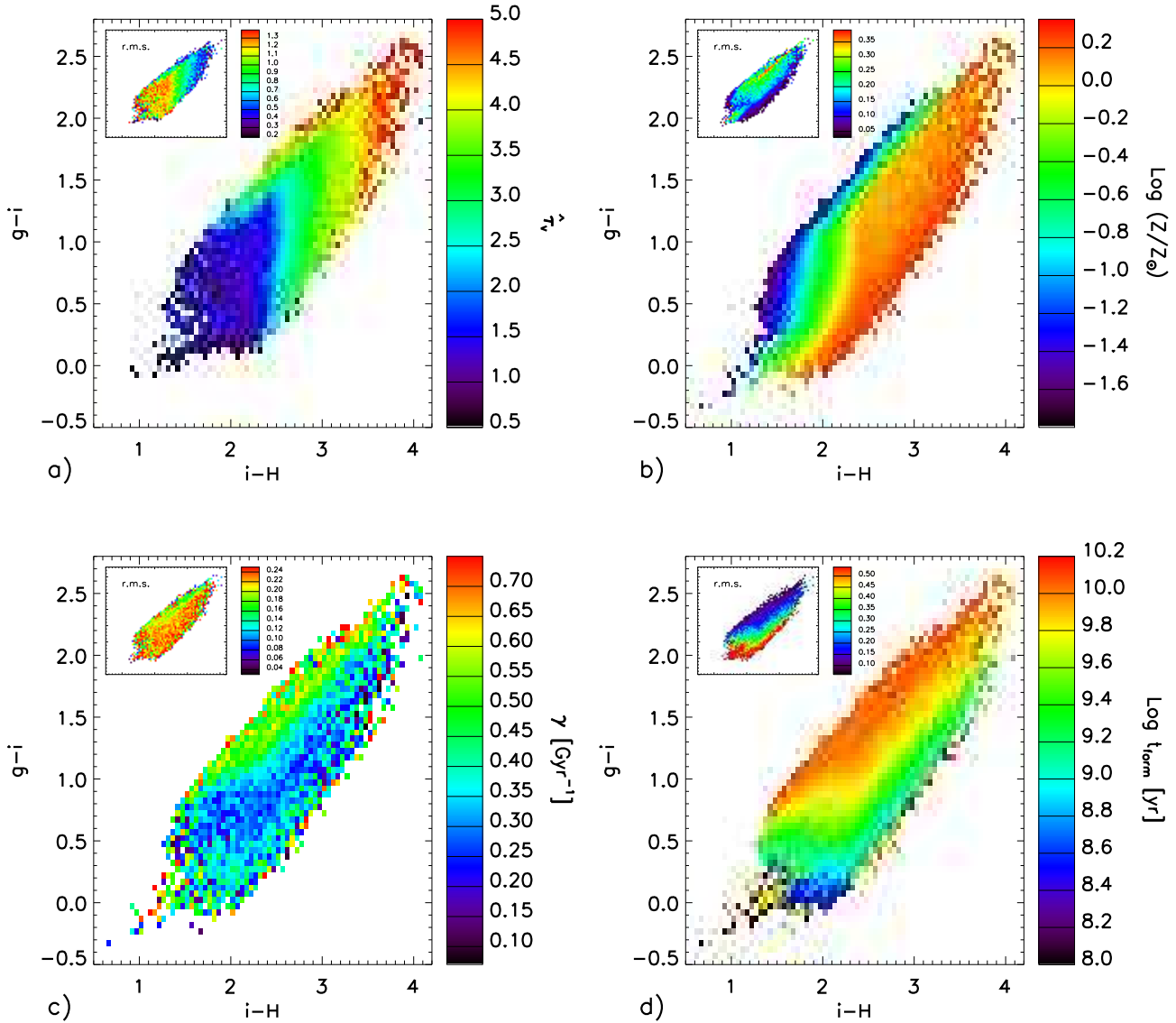


Figure A1. The median value of the input physical parameters of our library models as a function of $(g-i)-(i-H)$. The insets show the r.m.s. of the parameter values in each colour-colour bin. *Panel a*): the total effective optical depth of the dust in V -band, $\hat{\tau}_V$; *b*): the stellar metallicity, Z ; *c*): the inverse exponential time scale of the continuous component of the SFH, γ ; *d*): the time elapsed since the beginning of the SFH, t_{form} .

APPENDIX A: MODEL PHYSICAL PARAMETERS IN THE OPTICAL-NIR TWO-COLOUR SPACE

In this appendix we illustrate how distributed the models of our Monte Carlo SPS library are in the $(g-i)-(i-H)$ colour space in terms of input physical properties. We consider: the total optical depth of dust in V -band, $\hat{\tau}_V$; the metallicity, Z ; the inverse exponential time-scale of star formation, γ ; the time of formation of the first stars, t_{form} (taken as look-back time). Similarly to Fig. 1, each of the four main panels of Figure A1 show the median value of an input parameter for all models that end up in a given colour-colour bin. The insets show the corresponding r.m.s. We can easily distinguish two main regimes: *blue* models with $g-i \lesssim 1$ and $i-H \lesssim 2.3$, and all the rest. *Blue* models have the lowest $\hat{\tau}_V$ and $\gamma \lesssim 0.4 \text{Gyr}^{-1}$ corresponding to star-formation time scales longer than 2.5 Gyr, without any obvious dependence on colours and with a uniform large scatter. As opposed, the models in the *blue* regime span the whole range of t_{form} and metallicity, with an orthogonal systematic dependence on colours: older t_{form} correspond to redder $g-i$ irrespective of $i-H$, while higher metallicities correspond to redder $i-H$, almost independent on $g-i$. In the rest of the colour-colour space the change in colours appears to be largely driven by the dust, with the other three parameters being decisive only to determine the most extreme colours (i.e. at the edges of the distribution).

Table B1. Powerlaw fitting parameters for $\log \Upsilon_\lambda(\text{colour}) = a_\lambda + (b_\lambda \times \text{colour})$

Colour	a_g	b_g	a_r	b_r	a_i	b_i	a_z	b_z	a_J	b_J	a_H	b_H	a_K	b_K
$u - g$	-1.628	1.360	-1.319	1.093	-1.277	0.980	-1.315	0.913	-1.350	0.804	-1.467	0.750	-1.578	0.739
$u - r$	-1.427	0.835	-1.157	0.672	-1.130	0.602	-1.181	0.561	-1.235	0.495	-1.361	0.463	-1.471	0.455
$u - i$	-1.468	0.716	-1.193	0.577	-1.160	0.517	-1.206	0.481	-1.256	0.422	-1.374	0.393	-1.477	0.384
$u - z$	-1.559	0.658	-1.268	0.531	-1.225	0.474	-1.260	0.439	-1.297	0.383	-1.407	0.355	-1.501	0.344
$g - r$	-1.030	2.053	-0.840	1.654	-0.845	1.481	-0.914	1.382	-1.007	1.225	-1.147	1.144	-1.257	1.119
$g - i$	-1.197	1.431	-0.977	1.157	-0.963	1.032	-1.019	0.955	-1.098	0.844	-1.222	0.780	-1.321	0.754
$g - z$	-1.370	1.190	-1.122	0.965	-1.089	0.858	-1.129	0.791	-1.183	0.689	-1.291	0.632	-1.379	0.604
$r - i$	-1.405	4.280	-1.155	3.482	-1.114	3.087	-1.145	2.828	-1.199	2.467	-1.296	2.234	-1.371	2.109
$r - z$	-1.576	2.490	-1.298	2.032	-1.238	1.797	-1.250	1.635	-1.271	1.398	-1.347	1.247	-1.405	1.157

Colour	a_B	b_B	a_V	b_V	a_R	b_R	a_I	b_I	a_J	b_J	a_H	b_H	a_K	b_K
$B - V$	-1.330	2.237	-1.075	1.837	-0.989	1.620	-1.003	1.475	-1.135	1.267	-1.274	1.190	-1.390	1.176
$B - R$	-1.614	1.466	-1.314	1.208	-1.200	1.066	-1.192	0.967	-1.289	0.822	-1.410	0.768	-1.513	0.750

APPENDIX B: POWERLAW FITS TO M/L AS A FUNCTION OF ONE COLOUR

In Table B1 we report the parameters of powerlaw fits to the M/L in different bandpasses as a function of one optical colour:

$$\log \Upsilon_\lambda(\text{colour}) = a_\lambda + (b_\lambda \times \text{colour}) \quad (\text{B1})$$

This table is meant to provide a direct comparison with table 7 of Bell et al. (2003). Power-law fits to the M/L ratios of our CB07-based models are estimated by the following robust method: in first place models are binned in colour in intervals of 0.05 mag; for each bin the median M/L is computed and finally the power-law fit is computed via weighted linear least squares, where the number of models in each bin is adopted as weight. Magnitudes in the SDSS bands are meant to be in the AB systems, while for Johnson-Cousins filters they are expressed in Vega units.

As already discussed in the text, the slopes of our relations are significantly steeper than those computed by Bell et al. (2003) mainly because of the different assumptions about the star formation history, in terms of ages and bursts. For the reddest bandpasses the differences are even larger due to the new prescriptions for TP-AGB stars that are incorporated in our models.